A Coupled Ground Heat Flux-Surface Energy Balance Model of Evaporation Using Thermal Remote Sensing Observations

Bimal K. Bhattacharya[1*], Kaniska Mallick[2,3*], Devansh Desai[1,10,11], Ganapati S. Bhat[4], Ross Morrison[5], Jamie Clevery[6], Will Woodgate[7], Jason Beringer[8], Kerry Cawse-Nicholson[9], Siyan Ma[3], Joseph Verfaillie[3], Dennis Baldocchi[3]

[1]Agriculture & Land Ecosystem Division, Space Applications Center, ISRO, Ahmedabad, India

[2]Remote Sensing and Natural Resources Modeling, Department ERIN, Luxembourg Institute of Science and Technology, Belvaux, Luxembourg

[3]Environemtal Science Policy and Management, University of California, Berkeley, United States

[4]Centre for Atmosphere and Oceanic Studies, Indian Institute of Sciences, Bengaluru, India

[5]Centre for Ecology and Hydrology, Lancaster, UK

[6]Terrestrial Ecosystem Research Network, College of Science and Engineering, James Cook University, Cairns, Queensland, Australia

[7]CSIRO Land and Water, Private Bag 5, Floreat 6913, Australia.

[8]School of Earth and Environment, The University of Western Australia, WA, 6009, Australia

[9]Carbon Cycles and Ecosystems, Jet Propulsion Laboratory, California Institute of Technology, United States

[10]Department of Physics, Electronics & Space Sciences, Gujarat University, Ahmedabad, India

[11]Department of Physics, Institute of Science, Silver Oak University, Ahmedabad, Gujarat, India

Corresponding authors: Bimal K. Bhattacharya (bkbhattacharya@sac.isro.gov.in) and Kaniska Mallick (kaniska.mallick@gmail.com)

29   **Abstract**

30   One of the major undetermined problems in evaporation (ET) retrieval using thermal infrared

31   remote sensing is the lack of a physically based ground heat flux (G) model and its integration

32   within the surface energy balance (SEB) equation. Here, we present a novel approach based on

33   coupling a thermal inertia (TI)-based mechanistic G model with an analytical surface energy

34   balance model, Surface Temperature Initiated Closure (STIC, version STIC1.2). The coupled

35   model is named STIC-TI. The model is driven by noon-night (1:30 pm and am) land surface

36   temperature, surface albedo, and vegetation index from MODIS Aqua in conjunction with a clear-

37   sky net radiation sub-model and ancillary meteorological information. SEB flux estimates from

38   STIC-TI were evaluated with respect to the *in-situ* fluxes from eddy covariance measurements in

39   diverse ecosystems of contrasting aridity in both northern and southern hemispheres. Sensitivity

40   analysis revealed substantial sensitivity of STIC-TI-derived fluxes due to the land surface

41   temperature uncertainty. An evaluation of noontime G (G_i) estimates showed $12 – 21\%$ error across

42   six flux tower sites and a comparison between STIC-TI versus empirical G models also revealed

43   the substantially better performance of the former. While the instantaneous noontime net radiation

44   (R_{Ni}) and latent heat flux (LE_i) were overestimated (15% and 25%), sensible heat flux (H_i) was

45   underestimated (22%). Overestimation (underestimation) of LE_i (H_i) was associated with the

46   overestimation of net available energy ($R_{Ni} – G_i$) and use of unclosed SEB flux measurements in

47   LE_i (H_i) validation. The mean percent deviations in G_i and H_i estimates were found to be strongly

48   correlated with satellite day-night view angle difference in parabolic and linear pattern, and a

49   relatively weak correlation was found between day-night view angle difference versus LE_i

50   deviation. Findings from this parameter-sparse coupled G-ET model can make a valuable

51   contribution to mapping and monitoring the spatiotemporal variability of ecosystem water stress

52   and evaporation using noon-night thermal infrared observations from future Earth Observation

53   satellite missions such as TRISHNA, LSTM, and SBG.

54   **Keywords**: Thermal remote sensing, water stress, evaporation, ground heat flux, thermal inertia,

55   surface energy balance, STIC, terrestrial ecosystem

1 Introduction

One of the outstanding challenges in evaporation (ET) estimation through surface energy balance (SEB) model concerns an accurate characterization of ground heat flux in the open canopy architecture with mixed vegetation such as savanna or in ecosystems with low mean fractional vegetation cover, prevailing water stress, and strong seasonality in soil moisture. Ground heat flux (G) is an intrinsic component of SEB (Sauer and Horton, 2005), affecting the net available energy for ET (the equivalent water depth of latent heat flux, LE) and sensible heat flux (H). It represents an energy flow path that couples surface with the atmosphere and has important implications for the underlying thermal regime (Sauer and Horton, 2005). Depending on the vegetation fraction and water stress, the magnitude of instantaneous G varies greatly across different ecosystems. In the humid ecosystems with predominantly dense canopies and high mean fractional vegetation cover, G contributes to a small proportion in the surface energy balance. Dense canopy cover leads to less transmission of radiative fluxes through multiple layers of canopies, which results in low warming of the soil floor. Due to persistently high soil water content, humid ecosystems generally show low diurnal and seasonal variability in G. In contrast, the magnitude of G is substantially large in arid and semi-arid ecosystems with sparse and open canopy and soil moisture deficits. Due to prevailing feedback between the physics of ground heat flux, land-atmosphere interactions and vegetation ecophysiology, evaporation modelling in the complex ecosystems remains a challenging task (Wang et al., 2013; Kiptala et al., 2013). This paper addresses the challenge of simultaneous estimation of G and ET by combining thermal remote sensing observations with a mechanistic G model and a SEB model.

SEB models mainly emphasize on estimating sensible heat flux (H) by resolving the aerodynamic conductance (g_A) and computes LE as a residual SEB component as follows:

$$LE = R_N - G - H \qquad (1)$$

R_N is the net radiation. The proportion of R_N that is partitioned into G depends upon soil properties like its albedo, soil moisture, soil thermal properties such as thermal conductivity and heat capacity, which vary with mineral, organic and soil water fractions. SEB models use land surface temperature (LST or T_S) as an important lower boundary condition for estimating H and LE. Due to the extraordinarily high sensitivity of T_S to evaporative cooling and soil water content variations,

84   thermal infrared (TIR) remote sensing is extensively used in large scale evaporation diagnostics

85   (Kustas and Anderson, 2009; Mallick et al., 2014, 2015a, 2018a; Cammalleri and Vogt, 2015;

86   Anderson et al., 2012). Evaporation estimation through SEB models commonly employ empirical

87   sub-models of G in a stand-alone mode. Despite the utility of mechanistic G models is

88   demonstrated in different studies (Verhoef, 2004; Murray and Verhoef, 2007; Verhoef et al.,

89   2012), no TIR-based evaporation study attempted to couple a mechanistic G model with a SEB

90   model.

91   The SEB models for ET estimation driven by remote sensing observations generally use linear and

92   non-linear relationships for estimating G and such methods generally employ R_N, T_S, albedo (α_R),

93   and NDVI (e.g., Bastiaanssen et al., 1998; Friedl, 2002; Santanello and Friedl, 2003). While the

94   inclusion of T_S and albedo serves as a proxy for soil moisture and surface characteristics effects in

95   G, inclusion of NDVI provides a scaling of G - R_N ratio for different fractional vegetation cover.

96   Unfortunately, the empirical approaches do not include any information of soil temperature or

97   daily temperature amplitude. These empirical models also lack the universal consensus. Setting G

98   as a fraction of R_N does not solve the energy balance equation and disregards the role of thermal

99   inertia of the land surface (Mallick et al., 2015b). This could introduce substantial uncertainty in

100   LE estimation because G effectively couples the surface energy balance with energy transfer

101   processes in the soil thermal regime. It provides physical feedback to LE through the effects of

102   soil moisture, temperature, and conductivity (thermal and hydraulic) (Sauer and Horton, 2005).

103   Such feedbacks are most critical in the arid and semi-arid ecosystems where LE is significantly

104   constrained by the soil moisture dry-down. The limits imposed on LE by the water stress

105   consequently result in greater partitioning of the net available energy (i.e., R_N – G) into H and G

106   (Castelli et al., 1999).

107   When LE is reduced due to soil moisture dry-down, both G and T_S tend to show rapid intra-

108   seasonal rise. Therefore, the surface energy balance equation could be linked with mechanistic G

109   model, T_S harmonics (Verhoef, 2004), and soil moisture availability. Realizing the importance of

110   direct estimates of G in LE and invigorated by the advent of TIR remote sensing, Verhoef et al.

111   (2012) demonstrated the potential of a TI-based mechanistic model (Murray and Verhoef, 2007)

112   (MV2007 hereafter) for spatiotemporal G estimates in semi-arid ecosystems of Africa. Some

113   studies also emphasized the importance of using noontime and nighttime Ts and R_N for estimating

114   G (Mallick et al., 2015b; Bennet et al., 2008; Tsuang, 2005). The method of MV2007 has so far

115   been tested in a stand-alone mode, and no remote sensing method has so far been attempted to

116   combine such a mechanistic G model (e.g., MV2007-TI model) with a SEB model for coupled

117   energy-water flux estimation and validation.

118   By integrating T_S into a combined structure of the Penman-Monteith (PM) and Shuttleworth-

119   Wallace (SW) model, an analytical SEB model was proposed by Mallick et al. (2014, 2015a,

120   2016). The model, Surface Temperature Initiated Closure (STIC), is based on finding analytical

121   solution for aerodynamic and canopy-surface conductance (g_A and g_S) where the expressions of

122   the conductances were constrained by an aggregated water stress factor. Through physically

123   linking water stress (T_S derived) with g_A and g_S, STIC established direct feedback between T_S, H

124   and LE, and simultaneously overcame the need of empirical parameterization for estimating the

125   conductances (Mallick et al., 2016, 2018a). Different versions of STIC have been extensively

126   validated in different ecological transects (Tropical rainforest to woody savanna) and aridity

127   gradients (humid to arid) (Trebs et al., 2021; Bai et al., 2021; Mallick et al., 2015a; 2016; 2018a,

128   b; Bhattarai et al., 2018, 2019). Based on the conclusions of Verhoef et al. (2012), Mallick et al.

129   (2014; 2015a,b; 2016; 2018a,b, 2022), Bhattarai et al. (2018, 2019), and Bai et al. (2021), there is

130   a need to address some of the challenges in SEB modeling, which are, (i) accurate estimation of G

131   and ET in sparse vegetation, (ii) testing the utility of coupling a TI-based G model with an

132   analytical SEB model for accurately estimating G and ET, and (iii) detailed evaluation of a coupled

133   G-SEB model at the ecosystem scale. Realizing the significance of mechanistic G model

134   (MV2007), the advantage of the analytical STIC model, and to mitigate some of the overarching

135   gaps in SEB modeling in sparsely vegetated open canopy systems, this study presents the first-

136   ever coupled implementation of MV2007 G with the most recent version of STIC (STIC1.2). We

137   name this new coupled model as STIC-TI and it requires noon-night Ts and associated remotely

138   sensed land surface variables as inputs. We performed subsequent evaluation of STIC-TI in nine

139   terrestrial ecosystems in arid, semi-arid and sub-humid climate in India, the United States of

140   America (USA) (northern hemisphere) and Australia (southern hemisphere) at the eddy covariance

141   flux tower sites. The current study addresses the following research questions and objectives:

142 (i) What is the performance of STIC-TI G estimates when compared with conventionally used

143   empirical G models in ecosystems having low mean fractional vegetation cover (f_c) (≤0.5) and

144   having larger soil exposure to radiation for example in Savanna?

145 (ii) How do the estimates from STIC-TI LE and H fluxes compare with LE and H observations in

146   diverse terrestrial ecosystems that represent a varied range of f_c (0.25 – 0.5) covering cropland,

147   savanna, mulga vegetation (woodlands and open-forests dominated by the mulga tree [*Acacia*

148   *aneura*]) spread across arid, semi-arid, sub-humid, humid climates over a vast range of rainfall

149   (250 to 1730 mm), temperature (-4 to 46°C) and soil regimes?

150 (iii) What is the seasonal variability of G and evaporative fraction from STIC-TI model in a wide

151   range of ecosystems having contrasting aridity and vegetation cover?

152 It is important to mention that assessing the performance of STIC-TI LE and H with respect to

153 other SEB models is not within the scope of the present study. The prime focus of the current study

154 is to assess the sensitivity of STIC-TI, temporal variability of the retrieved SEB fluxes, and cross-

155 site validation of the individual SEB components.

156 A list of variables, their symbols and corresponding units are given in Table A1 in Appendix A.

157 **2 Study area and datasets**

158 **2.1Study site characteristics**

159 The present study was conducted using data from nine flux tower sites (four sites in India; three

160 sites in Australia; two sites in USA) equipped with Eddy Covariance (EC) measurement systems.

161 The distribution of the flux tower sites considered for the present study are shown in Fig.1 below.

162 The sites cover a wide range of climate, vegetation types, low fractional vegetation cover (f_c) of

163 around 0.5 and have contrasting aridity (Table 1). In India, a network of EC towers was set up

164 under Indo-UK INCOMPASS (INteraction of Convective Organization and Monsoon

165 Precipitation, Atmosphere, Surface and Sea*)* Program (Turner et al., 2019) at Jaisalmer (IND-Jai)

166 in Rajasthan state, Nawagam (IND-Naw*)* in Gujarat state, Samastipur (IND-Sam) in Bihar state

167 and under Newton-Bhaba programme (Morisson et al., 2019 a,b) at Dharwad (IND-Dha) in

168 Karnataka state. The flux footprint for EC towers in India varied from 500 m – 1 km (Bhat et al.,

169 2019). In the present study, about 90% of the fluxes came from an area within 500 m to 1 km from

170   the EC tower. Therefore, the relative contribution of vegetated land surface area to the fluxes is

171   close to 90% (Schmid, 2002; Vesala et al., 2008). The remaining percentage of fluxes originated

172   from an area beyond the flux footprint. The mean annual f_c was found to vary from 0.25 to 0.52

173   with standard deviation (SD) ranging from 0.1 to 0.16.

174   The IND-Jai site represents arid western zone over desert plains of natural grassland ecosystem.

175   The region receives very low rainfall (100 – 300 mm) during monsoon and experiences a wide

176   range in air temperature, high solar radiation, wind speed and high evaporative demand (Raja et

177   al., 2015). The IND-Naw site represents semi-arid agroecosystem in the middle Gujarat

178   agroclimatic zone of north-west India and has a pre-dominant rice-wheat cropping system. The

179   IND-Sam site has sub-humid climate of north-west alluvial plain zone in the Indo-Gangetic Plain

180   (IGP) situated in the eastern India and this site also follows rice-wheat crop rotation. IND-Dha

181   represents humid sub-tropical climate of transition zone in the southern India and this site

182   comprises of crops.
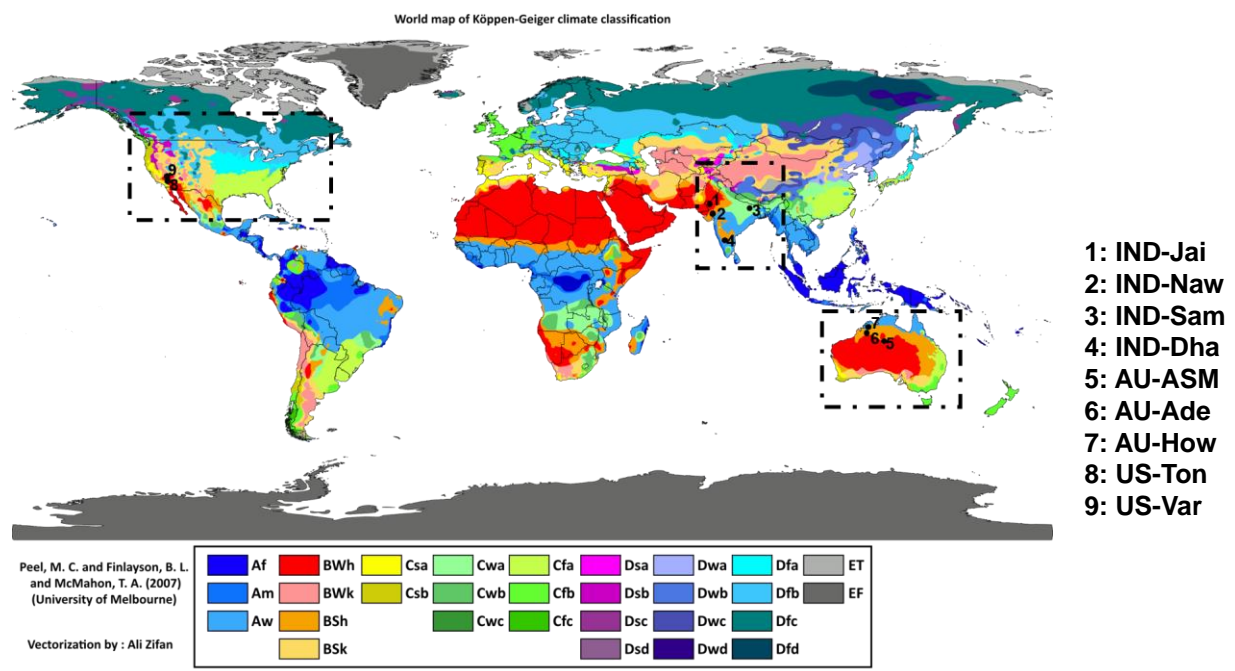
Figure 1: Locations of the flux tower sites in India, Australia and USA overlaid on climate type map. (Image Source: By Peel, M. C., Finlayson, B. L., and McMahon, T. A. (University of Melbourne) enhanced, modified, and vectorized by Ali Zifan; Hydrology and Earth System Sciences: "Updated world map of the Köppen-Geiger climate classification". Legend explanation, CC BY-SA 4.0, https://commons.wikimedia.org/w/index.php?curid=47086879)

In USA, two EC tower sites were located at Tonzi Ranch (US-Ton) and Vaira Ranch (US-Var), in the lower foothills of the Sierra Nevada Mountains. Both the EC stations are part of the AMERIFLUX Management Project (https://ameriflux.lbl.gov/). US-Ton is classified as an oak savanna woodland. While the overstorey is dominated by blue oak trees (40% of total vegetation) with intermittent grey pine trees (3 trees per hectare), the understory species include a variety of grasses and herbs. The mean annual rainfall at this site is 559 mm. US-Var is a grassland dominated site and the growing season is confined to the wet season only, typically from October to early May. The mean annual rainfall at this site is 559 mm. The mean annual f_c was found to vary from 0.18 to 0.26 and SD of the order of 0.06 to 0.07.

In Australia, three EC tower sites were located at Howard Springs (AU-How), Alice Springs Mulga (AU-ASM), Adelaide river (AU-Ade) in the Northern Territory as part of the OzFlux network (Beringer et al., 2016) and the Terrestrial Ecosystem Research Network (TERN), which is supported by the National Collaborative Infrastructure Strategy (NCRIS) (http://www.ozflux.org.au/monitoringsites/index.html). The AU-How is situated in the Black Jungle Conservation Reserve representing an open woodland savanna and the mean annual rainfall is 1750 mm. The AU-ASM is located on Pine Hill cattle station near Alice Springs. The woodland is characterized by mulga canopy and mean annual rainfall is 306 mm. AU-Ade represents savanna with a mean annual rainfall of 1730 mm. The mean annual f_c varied from 0.21 to 0.48 having SD range of 0.08 - 0.17. A description of Australian flux sites is given in Beringer et al. (2016). Average heights of vegetation are 1.15 m at IND-Naw, 1 m at IND-Jai, 1.23 m at IND-Sam, 1.5 m at IND-Dha, 6.5 m at AU-ASM, 15m at AU-How, 7 m at AU-Ade, 10 m at US-Ton, and ≤ 0.5 m at US-Var.

214 **Table 1:** An overview of the EC flux tower site characteristics in the present study

Hemisphere	Sites	Latitude (°N), Longitude (°E)	Climate & Vegetation	Mean f_c (SD)	Soil texture	T_A range (°C)	Mean Annual P (mm)	Observation period
Northern	Jaisalmer (IND-Jai)	26.99, 71.34	Arid grassland	0.25(±0.1)	Loamy fine sand to coarse sand	8 – 40	250	2017 – 2018
	Nawagam (IND-Naw)	22.80, 72.57	Semi-arid cropland	0.41(±0.13)	Sandy loam	9 – 39	700	2017 – 2018
	Samastipur (IND-Sam)	26.00, 85.67	Humid subtropical cropland	0.52(±0.16)	Sandy loam to loam	10 – 39	1000	2017 – 2018
	Dharwad (IND-Dha)	15.50, 74.99	Tropical Savanna	0.36(±0.11)	Shallow to medium black clay and red sandy loam soils	12 – 40	650	2016 – 2018
	Tonzi ranch (US-Ton)	38.43, -120.96	Woody Savanna	0.18(±0.06)	Red sandy clay loam	0 – 40	559	2011 – 2019
	Vaira ranch (US-Var)	38.41, -120.95	Arid grassland	0.26(±0.07)	Rocky silt loam	0 – 40	559	2011 – 2019
Southern	Alice Springs Mulga (AU-ASM)	-22.28, 133.24	Semi-arid mulga	0.21(±0.09)	Loamy sand	(-4) – 40	305	2011 – 2014
	Howard Springs (AU-How)	-12.49, 131.15	Tropical savanna	0.48(±0.17)	Red kandasol	19 – 34	1700	2011 – 2014
	Adelaide River (AU-Ade)	-13.07, 131.11	Savanna	0.42(±0.08)	Yellow hydrosol, shallow, loamy sand with coarse gravel	16 – 37	1730	2007 – 2009

215   T_A: Air temperature during the observation period; P: rainfall (mm) measured using rain gauge at flux tower site during the study
216   period. IND is for India, AU is for Australia, and US is for the United States; SD is standard deviation of annual mean fc which is
217   computed from NDVI as mentioned in section 3.1.

9

2.2 Datasets

2.2.1 Micrometeorological data at flux tower sites

Standardized, controlled, and harmonized surface energy balance (SEB) flux and meteorological data from nine EC towers were used in the present analysis. In Australia, H and LE were measured through the EC systems and R_N were measured through net radiometers at varying heights of 15 m (AU-Ade), 23 m (AU-How), and 11.6 m (AU-ASM), respectively. In India, the EC measurement height was maintained approximately at 8 m above the surface, except at IND-Dha where it was installed at a height of 4.2 m. In USA, the SEB measurements were carried out at tower heights of 23 m at US-Ton and 2 m US-Var. A summary of the instrumentation is given in Table A2 of Appendix A. All the flux tower sites were equipped with a range of meteorological instrumentation which measured diurnal air temperature (T_A) and relative humidity (R_H), four components of the net radiation (R_N, consisting of down- and up-welling shortwave and long-wave radiation (SW↓, SW↑, LW↑ and LW↓, respectively)) above the vegetated canopy. In addition, the diurnal soil heat flux (G) and soil temperature (T_{ST}) were measured at all the three Australian sites and two US sites. In India, the diurnal soil heat flux was measured only at IND-Dha.

For the Indian sites, the raw EC measurements of the turbulent wind vectors (*u*, *v* and *w*, for horizontal, meridional and vertical, respectively), sonic temperature (T), and CO_2 and water vapor mass density were recorded at a sampling rate of 20 Hz. Raw EC data were post-processed to obtain level-3 quality controlled and harmonized surface fluxes at 30-minute flux averaging intervals using EddyPRO® Flux Calculation Software (LI-COR Biosciences, Lincoln, Nebraska, USA) using the data handling protocol described by Bhat et al. (2019). The EC data from the OzFlux sites was averaged over 30 minutes recorded by the logger and processed through levels using the PyFluxPro standard software processing scripts as mentioned in Isaac et al. (2017). The Level 3 (L3) used in this paper was produced using PyFluxPro (Isaac et al., 2017) employing the Dynamic INtegrated Gap filling and partitioning for Ozflux (DINGO) system as described in Donohue et al. (2014) and Beringer et al. (2016).The quality checked EC data at 30 minute intervals for two AMERIFLUX sites US-Ton and US-Var was acquired from *https://doi.org/10.17190/AMF/1245971&https://doi.org/10.17190/AMF/1245984*, respectively.

2.2.2 Remote sensing data

247 Optical and thermal remote sensing observations available from Moderate Resolution Imaging

248 Spectroradiometer (MODIS) (Didan et al., 2015) on-board Aqua platform were used in the present

249 study (Table 2) for estimating G and associated SEB fluxes. These include eight-day land surface

250 temperature (LST or T_S) at 1:30 pm and 1:30 am, and surface emissivity (ε_s) (MYD11A2), daily

251 surface albedo (α_R) (MCD43A3), 16-day NDVI (MYD13A2). The overpass times of MODIS

252 Aqua are at 1:30 pm and 1:30 am. The 8-day average values of clear-sky T_S available from

253 MYD11A2 data were used (Source: https://vip.arizona.edu/documents/viplab/MYD11A2.pdf) for

254 all nine flux tower sites. Since MYD21A2 LST product is known to provide better accuracy (1 –

255 1.5 K) (Hulley et al, 2016) as compared to MYD11A2 LST over semi-arid and arid ecosystems,

256 the former was also used in STIC-TI to compare LE and H estimates (see Table 5 in section 4.4)

257 with the estimates of MYD11A2 LST over the arid and semi-arid sites (IND-Jai, IND-Naw, US-

258 Ton). The noon-night pair of thermal remote sensing observations from Aqua are close to the time

259 of occurrences of maximum and minimum soil surface temperature (see Figure 2) and are therefore

260 ideal for soil heat flux modeling using thermal inertia. The MODIS Terra overpass times are at 11

261 am and 11 pm and are far from the time of occurrences of minimum-maximum soil temperatures.

262 Therefore, MODIS Aqua acquisition times were used in the present study.

263 **Table 2:** A summary of MODIS Aqua optical and thermal remote sensing products used in the
264 present study

Data type	Product ID (version)	Variables used	Spatial resolution (m)	Temporal resolution	Purpose	Inputs to equation numbers
LST and emissivity	MYD11A2 (V006) MYD21A2	T_S (1:30 pm and am) and ε_s	923	8-day	For estimating R_{Ni}, G_i, LE_i, H_i	(5), (13), (C6), (C7), (B8)
Surface albedo	MCD43A3 (V006)	α_R	462	8-day composite from daily	For estimating R_{Ni}, G_i	(5), (B3)

Vegetation index	MYD13Q1 (V006)	NDVI	250	16-day	For estimating G_i	(4)

3 Methodology

3.1 Coupled soil heat flux-SEB model

In this paper, we modified a thermal inertia (TI) based soil heat flux (G) model using noon-night thermal remote sensing observations and thereafter coupled the TI-based G with STIC1.2. A clear-sky net radiation (R_N) model was also introduced into this coupled model and R_N estimation algorithm is described in Appendix B. The estimation of G through modifying MV2007-TI approach and its coupling with STIC1.2 is the most novel component of the modeling scheme, and it is therefore described in the main body of the paper (section 3.1.1). Such a coupling enabled the implementation of a mechanistic G model along with an analytical SEB model using optical-thermal remote sensing data. The coupled model is hereafter referred as STIC-TI.

3.1.1 MV2007 soil heat flux model based on Thermal Inertia (TI)

The functional form for estimating instantaneous G (G_i, hereafter) (eq. 2 below) is based on the harmonic analysis of soil surface temperature and is described in detail by Murray and Verhoef (2007) and Maltese et al. (2013).

$$G_i = \Gamma\left[(1 - 0.5f_C)\left(\sum_{n=1}^{k} A\sqrt{n\omega}\sin\left(n\omega t + \phi'_n + \frac{\pi}{4} - \frac{\pi\Delta t}{12}\right)\right)\right] = \Gamma J_S \qquad (2)$$

G_i is the soil heat flux at the surface at a particular instance (Wm^{-2}), Γ is the soil thermal inertia (J m^{-2} K^{-1} s$^{-0.5}$), k is the total number of harmonics used, A is the amplitude (°C) of the nth soil surface temperature (T_{ST}) harmonic, ω is the angular frequency (rads^{-1}), t is the time (s), ϕ'_n is the phase shift of the nth soil surface temperature harmonic (rad), J_S is the summation of harmonic terms of soil surface temperature (K), and Δt(s) is time offset between the canopy composite temperature and the below-canopy soil surface temperature. Here, we represent G_i and A as ecosystem-scale ($\leq$ 1km) soil heat flux and surface soil temperature amplitude (averaged from soil surface to 10 cm depth), respectively and assume it to be valid for different vegetated landscape.

287 Since we have considered a single pair (noon-night corresponding to 1:30 pm and 1:30 am) of

288 MODIS aqua LST data in the present study, the phase shift (ϕ'_n) is taken as zero and number of

289 harmonics is taken as one (k=1) for estimating G_i. Thus equation (2) is modified as follows:

$$G_i = \Gamma\left[(1 - 0.5f_C)\left(A\sqrt{\omega}\sin\left(\omega t + \frac{\pi}{4} - \frac{\pi\Delta t}{12}\right)\right)\right] = \Gamma J_S \qquad (3)$$

290 With the two boundary values (i.e., Δt =1.5 h for $f_c = 1$ and $\Delta t = 0$ for $f_c = 0$, f_c being the vegetation

291 fraction), a linear approach is proposed here to describe the time offset Δt as a function of f_c

292 (Maltese et al., 2013). For a given day, f_c was derived by normalizing NDVI with the upper-lower

293 limits of annual NDVI cycle.

$$\Delta t = 1.5\ f_c \qquad (4)$$

3.1.1.1 Scaling function for estimating ecosystem-scale surface soil temperature amplitude (A)

295 Estimating ecosystem-scale A involves two steps, (a) computing point-scale soil surface

296 temperature amplitude (from surface to 0.1m depth) (T_{STA}, hereafter) from the available

297 measurements of soil surface temperature, and (b) linking T_{STA} with remote sensing variables to

298 develop scaling functions for A. Point-scale soil temperature measured at different depths within

299 top 10 cm soil layer at AU-ASM, US-Ton, US-Var was averaged and considered as representative

300 surface soil temperature (0 – 10 cm). For Ind-Dha and AU-Ade, single-depth (10 cm) soil

301 temperature measurement was used. Studies also showed that LST carries some signal beneath the

302 skin of the surface (Johnston et al., 2022).

303 Several studies suggested theoretical sinusoidal trajectory of soil surface and sub-surface

304 temperatures (Gao et al., 2010), where the amplitude is maximum at the surface, and it gradually

305 decreases with depth to become 37% of surface amplitude until the damping depth (Hillel, 1982).

306 However, at deeper depths, soil temperatures remain constant with time and do not show many

307 fluctuations as compared to surface or near-surface soil temperatures. This invariant soil

308 temperature is called deep soil temperature (Mihailovic et al., 1999). However, the diurnal surface

309 soil temperature measurements (within top 0.1 m depth) across different flux tower sites showed

310 a sinusoidal-exponential behavior, i.e., sinusoidal pattern from sunrise until the afternoon and

311 exponential pattern from afternoon through sunset to the next sunrise. An illustrative example of

312   the theoretical and observed trajectories of surface soil temperature is shown in Fig. 2. This diurnal

313   surface soil temperature variation has a single harmonic component (Gao et al., 2010). For

314   computing T_{STA}, theoretical half-curve of sinusoidal pattern is assumed and was derived from

315   measurements as exemplified in Fig 2.
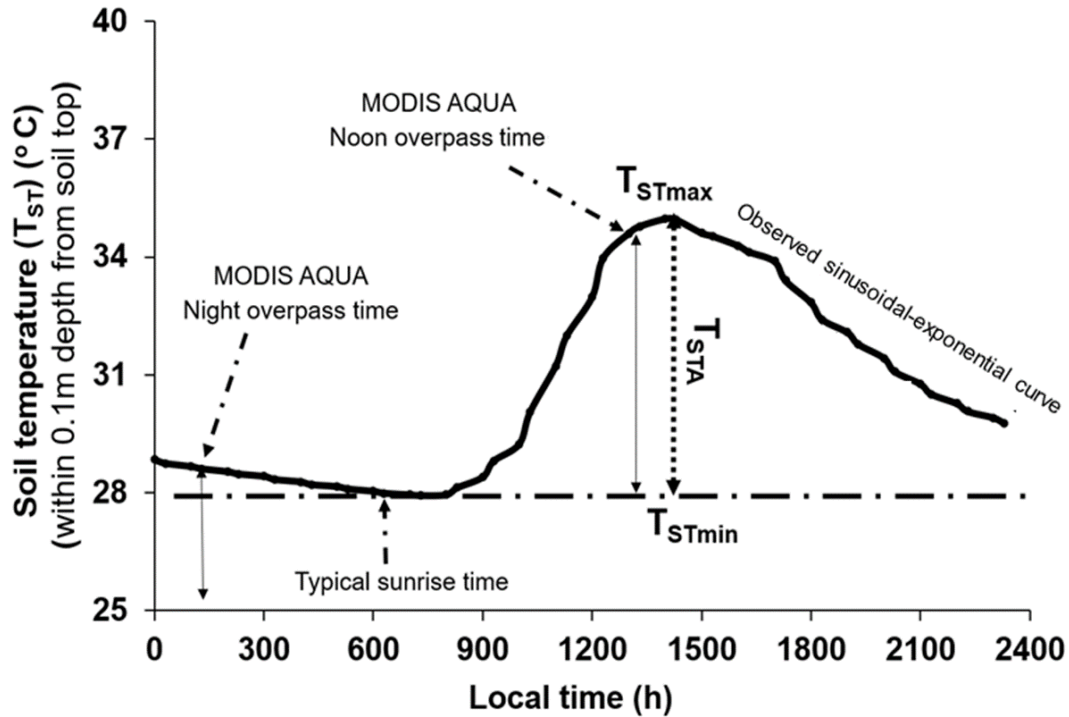
Figure 2. An illustrative example of typical diurnal variation of observed soil temperature (T_{ST}) (from surface to 0.1m depth) at OzFlux sites and timings of MODIS AQUA observations. Here, T_{STmax} and T_{STmin} are maximum and minimum point-scale observed soil surface temperatures

316

317   It is evident from Fig. 2 that T_{STmin} represents minimum surface soil temperature occurring 1-1.5h

318   after sunrise and T_{STmax} occurs during 12.30 – 15.00h local time. The *in-situ* measured T_{ST} on

319   completely clear-sky days at OzFlux sites were used to extract T_{STmax} and T_{STmin} and T_{STA} was

320   derived as (T_{STmax}- T_{STmin}) from the theoretical half-curve of sinusoidal pattern.

321   T_{STA} is generally influenced by several land surface characteristics such as surface temperature

322   and surface albedo of soil-canopy complex, surface heat capacities, fractional canopy cover and

323   thermal conductivity (White, 2013). T_S and α_R are the major thermal and reflective land surface

324   properties that have strong synergy with surface soil temperature dynamics. Hence, we have used

325   bivariate regression analysis to develop a scaling function for estimating ecosystem-scale T_{STA} (top

326   to 0.1m depth). The bivariate regression is based on the difference of noon (d) and night (n) T_S

14

327 data and α_R (Duan et al., 2013, Li Tian et al., 2014) from MODIS Aqua. The scaling function given

328 in eq. (5) estimates ecosystem-scale T_{STA} (symbolized as 'A' in equation 5) from surface to 0.1 m

329 soil depth:

$$A = B_1(T_{Sd} - T_{Sn}) + B_2(\alpha_R) + B_3 \qquad (5)$$

330 Here, B1, B2, B3 are coefficients of regression model; T_{Sd} and T_{Sn} are noon and nighttime LST,

331 respectively. The results of this regression analysis are elaborated in section 4.1.

3.1.1.2 Estimating Γ

333 Γ is the key variable for estimating G_i using eq. (2). MV2007 adopted the concept of normalized

334 thermal conductivity (Johansen, 1975) and developed a physical method to estimate Γ as follows:

$$\Gamma = e^{\left[\Upsilon'\left(1 - S_r^{(\Upsilon' - \delta)}\right)\right]}(\tau_* - \tau_0) + \tau_0 \qquad (6)$$

335 where τ_* and τ_0 are the thermal inertia for saturated and air-dry soil (J m^{-2}K^{-1}s$^{-0.5}$); $\tau_0 = D_1\theta_* + D_2$;

336 $\tau_* = D_3 (\theta_*^{-1.29})$; Υ' (−) is a parameter depending on the soil texture (Murray and Verhoef, 2007;

337 Minasny, 2007; Anderson et al., 2007); S_r (m^3 m^{-3}) is relative saturation and is equal to (θ/θ_*); δ

338 (unitless) is the shape parameter which is dependent on the soil texture. θ_* (m^3 m^{-3}) is the soil

339 porosity (equal to the saturated soil moisture content when soil moisture suction is zero), θ (cm^3

340 cm^{-3}) is the volumetric soil moisture and D_1, D_2, D_3 are coefficients which were derived from a

341 large number of experimental data. The reported global values of D_1, D_2, and D_3 were taken as -

342 1062.4, 1010.8, 788.2, respectively (Maltese et al., 2013). The value for θ_* and shape parameter

343 for soil textures across study sites were specified according to Van Genuchten et al. (1980). The

344 details are mentioned in Table E1 of Appendix E.

345 In the present study, the relative soil moisture saturation, S_r (θ/θ_*) is represented in terms of an

346 aggregated moisture availability (M) of canopy-soil complex through a linear function (eq. 12). In

347 case of zero canopy cover, M represents the soil moisture availability from surface to 0.1 m depth.

348 In sparse and open canopy, rates of moisture availability from soil to root and root to canopy were

349 assumed same.

350   Theoretically, M is expressed as available soil moisture fraction between field capacity (θ_{fc}) and

351   permanent wilting (θ_{wp}) point as given in eq. (7) below.

$$M = \frac{\theta - \theta_{wp}}{\theta_{fc} - \theta_{wp}} \tag{7}$$

352   Where, θ_{fc} ($m^3\ m^{-3}$) is the volumetric soil moisture at the field capacity (at a suction of 330 hPa)

353   and θ_{wp} ($m^3\ m^{-3}$) is the volumetric soil moisture at the permanent wilting point (at suction of 15000

354   hPa) (Singh, 2007). Since θ_{fc}, θ_*, θ_{wp} are characteristic volumetric soil moisture contents

355   corresponding to specific suctions and depends on the soil texture, dividing the numerator and

356   denominator in eq. (7) by θ_* gives the following expression:

$$M = \frac{\dfrac{\theta}{\theta_*} - \dfrac{\theta_{wp}}{\theta_*}}{\dfrac{\theta_{fc}}{\theta_*} - \dfrac{\theta_{wp}}{\theta_*}} \tag{8}$$

357   Due to their dependence on soil texture, the ratios (θ_{fc}/θ_*) and (θ_{wp}/θ_*) are treated as constants.

358   These are represented as C and C′ in the later equations (eq. 9, 10, and 11). The constants, C and

359   C′ vary from 0.3 to 0.8 and from 0.1 to 0.4 (Murray and Verhoef, 2007; Minasny et al., 2011;

360   Anderson et al., 2007), respectively over different soil textures.

$$M = \frac{\dfrac{\theta}{\theta_*} - C'}{C - C'} \tag{9}$$

$$M(C - C') = \left(\frac{\theta}{\theta_*}\right) - C' \tag{10}$$

361   By replacing S_r in eq. (6) as θ/θ_* and by rearranging eq. (10), the following linear function is

362   obtained.

$$S_r = \frac{\theta}{\theta_*} = M\ (C - C') + \ C' = M' \tag{11}$$

363   Thus, the modified equation to calculate Γ is given by eq. (12) as follows:

$$\Gamma = e^{\left[\Upsilon'\left(1 - M'^{(\Upsilon' - \delta)}\right)\right]}(\tau_* - \tau_0) + \tau_0 \tag{12}$$

364   By substituting the values obtained from eq. (4), (5) and (12) into eq. (3), we obtained the
365   instantaneous ecosystem-scale G_i corresponding to MODIS Aqua noontime overpass. The intrinsic
366   link between G_i estimates through MV2007-TI and SEB scheme in STIC1.2 is made through M,
367   where the computation of M follows the procedure as described in Mallick et al. (2016, 2018a, b)
368   and Bhattarai et al. (2018). (description in Appendix C).

369   ### *3.1.1.3 Estimating M*

370   In STIC1.2, an aggregated moisture availability (M) of canopy-soil complex is expressed as the
371   ratio of the 'vapor pressure difference' between the aerodynamic roughness height of the canopy
372   (i.e., source/sink height) and air to the 'vapor pressure deficit' between aerodynamic roughness
373   height to the atmosphere:

$$M = \frac{(e_0 - e_A)}{(e_0^* - e_A)} = \frac{(e_0 - e_A)}{\kappa(e_S^* - e_A)} = \frac{s_1(T_{0D} - T_D)}{\kappa s_2(T_S - T_D)} \tag{13}$$

374   Where e_0 and e_0^* are the actual and saturation vapor pressure at the source/sink height; e_A is the
375   atmospheric vapor pressure; e_S^* is the saturation vapor pressure at the surface; T_{0D} is dew point
376   temperature at the source/sink height; T_S is the LST; T_D is the air dew point temperature; s_1 and s_2
377   are the psychrometric slopes of the saturation vapor pressure and temperature between $(T_{0D} - T_D)$
378   versus $(e_0 - e_A)$ and $(T_S - T_D)$ versus $(e_S^* - e_A)$ relationship; and κ is the ratio between $(e_0^* - e_A)$
379   and $(e_S^* - e_A)$. To solve the eq. (13), estimation of T_{0D} is necessary. An initial estimate of T_{0D} [T_{0D}
380     $= [(e_S^* - e_A) - s_3 T_S + s_1 T_D]/(s_1 - s_3)]$ and M were obtained following Venturini et al. (2008) where
381   s_1 and s_3 were approximated in T_D and T_S, respectively. However, eq. (13) cannot be directly
382   solved because there are two unknowns in one equation. However, since T_{0D} also depends on LE
383   (Mallick et al., 2016, 2018a), an iterative updation of T_{0D} (and M) was carried out by expressing
384   T_{0D} as a function of LE [$T_{0D} = T_D + (\gamma LE/\rho c_p g_A s_1)$] which is described in detail by Mallick et al.
385   (2016, 2018a) and Bhattarai et al. (2018). In the numerical iteration, s_1 was not updated to avoid
386   numerical instability and it was expressed as a function of T_D.

3.1.2 STIC-TI: Coupling modified MV2007-TI and STIC 1.2

The initiation of the coupling between MV2007-TI and STIC1.2 was executed through linking G_i estimates from the modified MV2007-TI with M estimates from STIC1.2. Having the initial estimates of M (through eq. 13), an initial estimation of G_i was made from eq. (2) where S_r in eq. 11 was replaced with the initial estimates of M'. From the initial estimates of G_i (eq. 2) and R_{Ni} (equations in Appendix B), initial estimates of LE_i and H_i were obtained through the Penman-Monteith Energy Balance (PMEB) equation. Analytical expressions of the conductances for estimating H and LE through the PMEB equation were obtained by solving the state equations as described in the Appendix. The process was then iterated by updating T_{0D} [$T_{0D} = T_D + (\gamma LE / \rho c_p g_{AS_1})$] and M in every time step (as mentioned in Mallick et al., 2016, 2018a), and re-estimating G_i (using eq. 3), net available energy ($R_{Ni} - G_i$), conductances, LE_i and H_i, until stable estimates of LE_i were obtained. The conceptual block diagram and algorithm flow of STIC-TI is shown in Fig. 3a and Fig 3b, respectively.
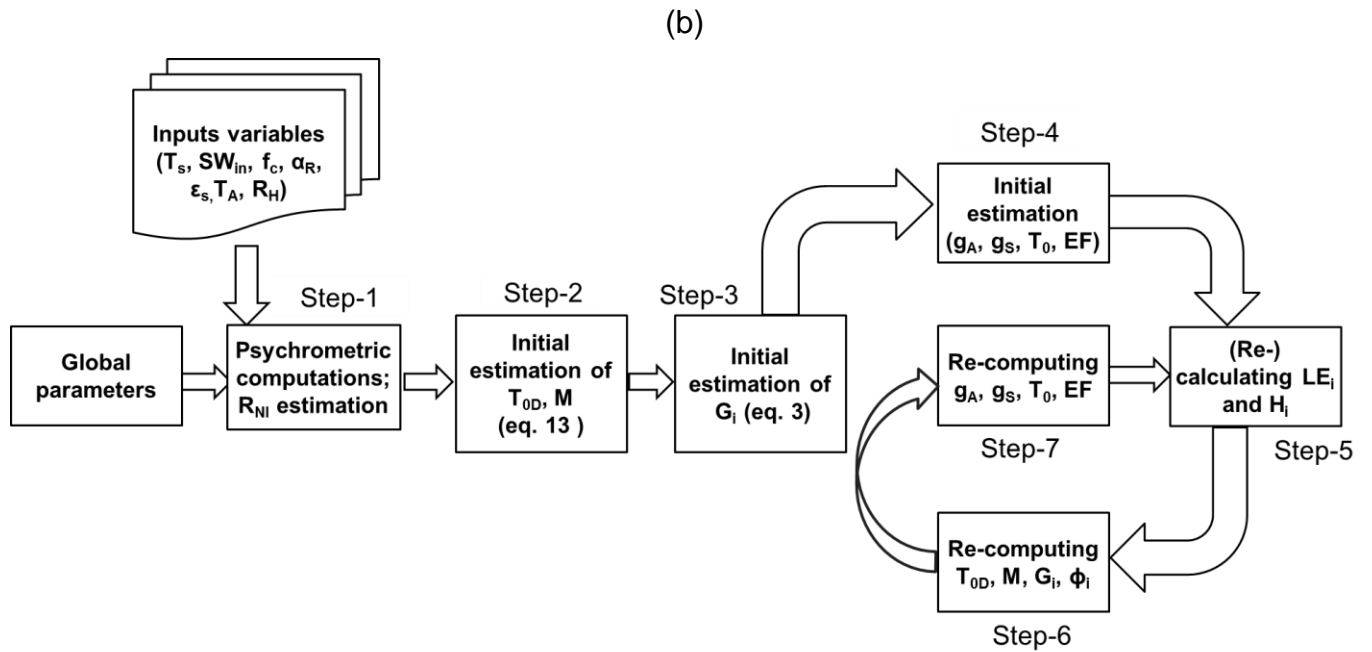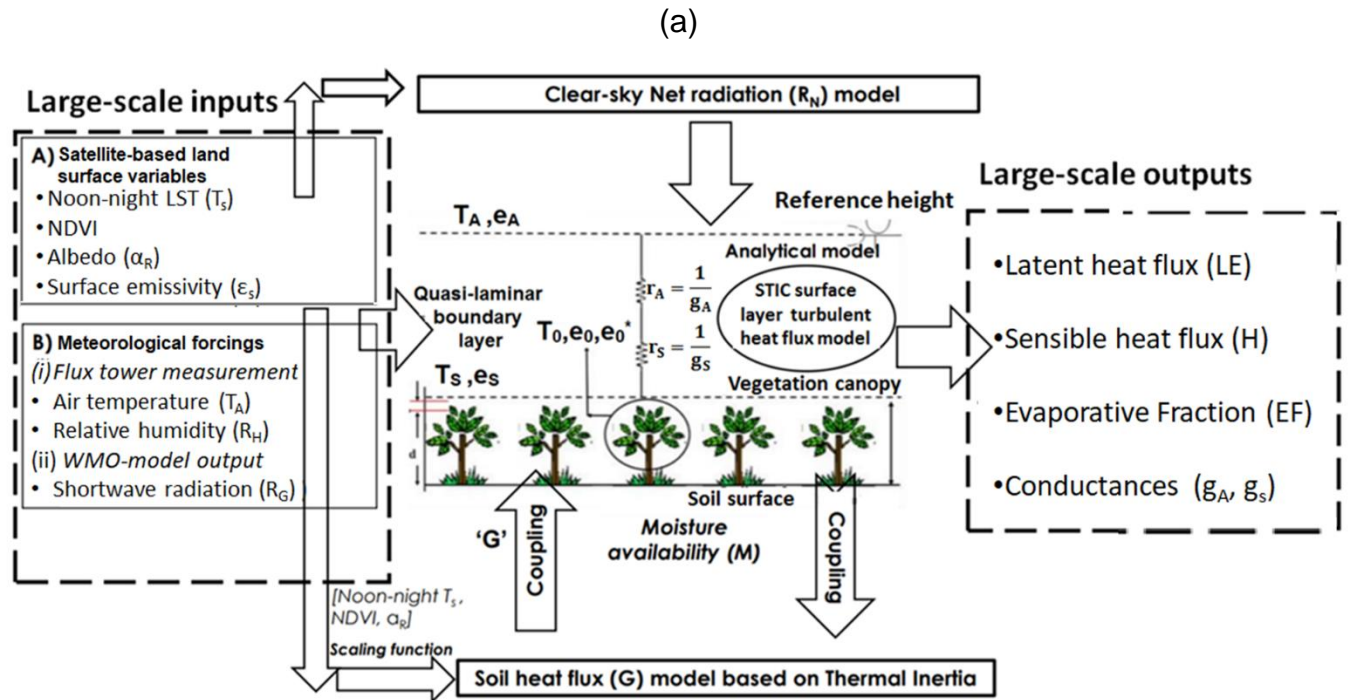
(a)

(b)

Figure 3: (a) Conceptual diagram of STIC-TI model showing different input variables and model outputs, (b) Algorithmic flow for estimating G and associated SEB fluxes through STIC-TI.

406   Examples of iterative stabilization of G_i and LE_i for Indian, Australian and US ecosystems of India

407   are shown in Fig. 4. The iterative stabilization of G_i and LE_i was obtained between 8-25 iterations

408   for all sites.
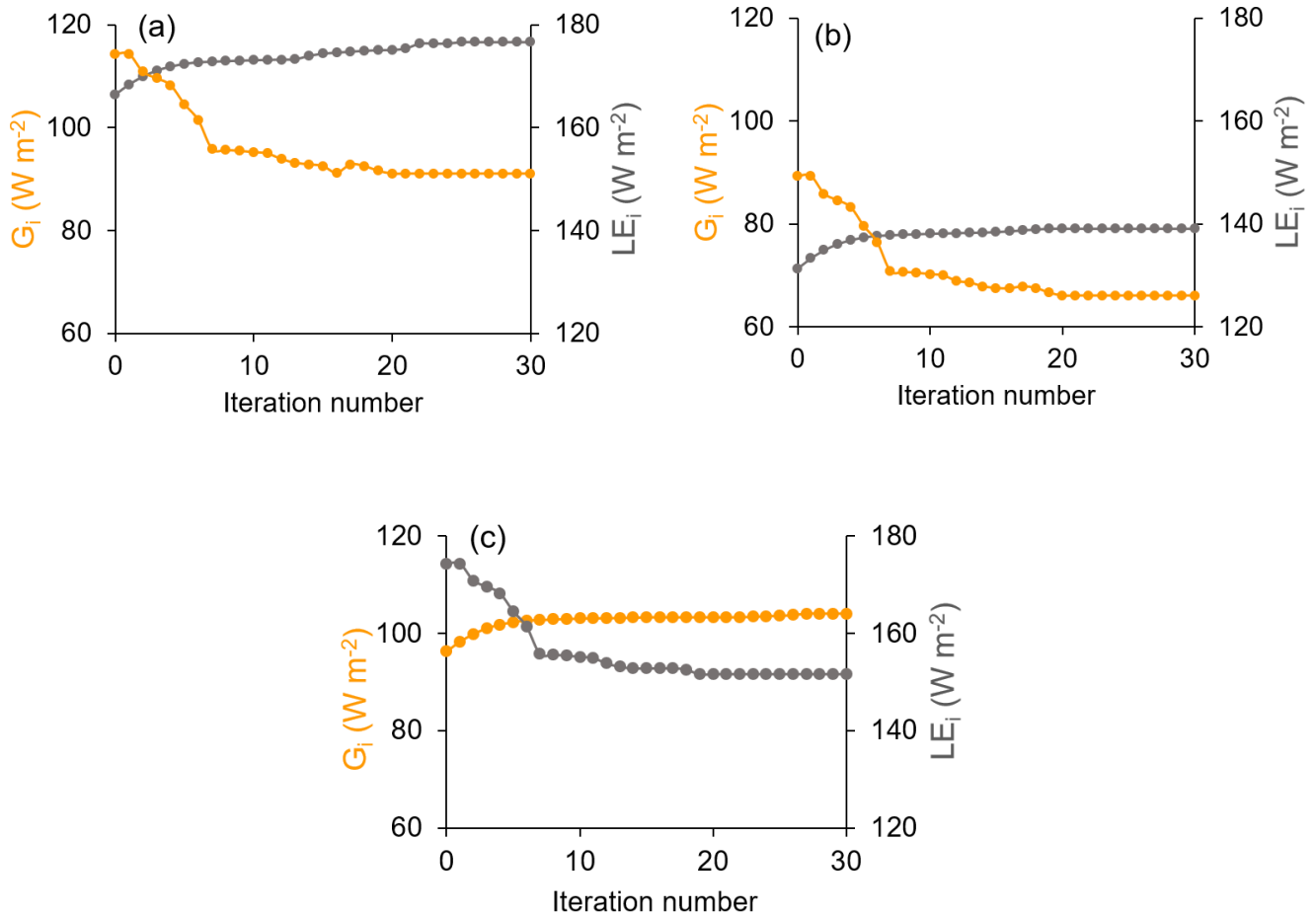
Figure 4: Illustrative examples of iterative stabilization of STIC-TI G_i (yellow marker line) and LE_i (grey marker line) in (a) IND-Jai, (b) AU-ASM, (c) US-Ton

409

410   The noteworthy features of STIC-TI are: (1) estimating G by modifying the mechanistic MV2007-

411   TI model using noon and midnight T_S information from thermal remote sensing observations

412   available through polar orbiting satellite platform (e.g. MODIS Aqua), (2) coupling the

413   mechanistic MV2007-TI G model with STIC1.2 to simultaneously estimate surface moisture

414   availability (M), G, and SEB fluxes, (3) introducing water stress information in G (through M) to

415   better constrain the aerodynamic and canopy-surface conductances as well as the SEB fluxes, and

416 (4) derivation of amplitude of ecosystem-scale surface soil temperature (from top soil to 0.1 m soil
417 depth).

3.1.3 Generation of remote sensing inputs

419 Two of the key variables in SEB modeling are Ts and ε_s. These two variables were retrieved at
420 923m spatial resolution from MODIS Aqua noon-night TIR observations (MYD11A2) in bands
421 11.03 µm and 12.02 µm using a generalized split-window algorithm (Wan et al., 2015). For
422 optimal retrieval, tractable sub-ranges of atmospheric column water vapor and lower boundary air
423 surface temperature were used. Land surface emissivity was estimated from land cover types and
424 anisotropy factors. The MYD21A2 LST product was generated using Temperature-Emissivity
425 Separation (TES) algorithm (Hulley et al, 2016) and improved water vapor scaling method to
426 remove the atmospheric effects. Albedo was estimated from MODIS (MCD43A2 Version 6.0)
427 Bidirectional Reflectance Distribution Function and Albedo (BRDF/Albedo) daily dataset (Schaaf
428 et al., 2002)) at 462 m spatial resolution. Actual albedo is a value which is interpolated between
429 white-sky and black-sky albedo as a function of fractional diffuse skylight (which is a function of
430 aerosol optical depth). NDVI was obtained from level 3 MODIS vegetation indices product
431 (MYD13Q1, version 6.1), which are generated every 16-day at 250 meter (m) spatial resolution.
432 All the input remote sensing variables mentioned in table 2 were resampled to spatial resolution
433 of MYD11A2 product (923 m).

3.2 Sensitivity and statistical analysis

435 The accuracy of STIC-TI heavily depends on the accuracy of T_S, NDVI, and α_R due to the dual
436 role of T_S in estimating M and G_i, the role of NDVI in G_i, and the combined role of T_S and α_R in
437 estimating R_{Ni}. Therefore, one-dimensional sensitivity analysis was conducted to assess the
438 impacts of uncertainty in T_S, NDVI and α_R on G_i, H_i and LE_i. The sensitivity was assessed by
439 varying noon-time T_S by ±0.5 K, ±1.0 K and ±1.5 K (keeping nighttime T_S constant so that
440 amplitude can vary automatically); varying NDVI by ±0.05; ±0.10, ±0.15; and varying albedo by
441 ±0.02, ±0.05, ±0.10, respectively. SEB fluxes were computed by using T_S, NDVI, and α_R for three
442 different periods of the year in all the eight ecosystems. Sensitivity analyses were conducted by
443 increasing and decreasing systematically T_S, NDVI, α_R from its central value while keeping the
444 other variables and parameters constant. This procedure was selected because the fluxes and

445   intermediate outputs of the STIC-TI model reflect an integrated effect due to uncertainty in T_S. In

446   the first run, SEB fluxes were computed using *in-situ* T_S measurements obtained from the flux

447   tower outgoing longwave radiation measurements. Then T_S was increased and decreased at

448   constant interval and a new set of fluxes were estimated. In the similar way, α_R and NDVI were

449   increased and decreased at constant intervals and new set of fluxes were computed. The sensitivity

450   of STIC-TI was assessed by the equation 14.

$$\text{Sensitivity} = \frac{E_{i0} - E_{iM}}{O_i} * 100 \tag{14}$$

451   E_{i0} is the estimated (original) model output and E_{iM} is the estimated (modified) output obtained by

452   changing the variable whose sensitivity is to be tested. O_i is actual measurements. Apart from the

453   sensitivity analysis, the following set of statistical metrics were used to assess model performances.

$$R^2 = \left(\frac{\sum_{i=1}^{n}(E_i - \bar{E})(O_i - \bar{O})}{\sqrt{\sum_{i=1}^{n}(E_i - \bar{E})^2} \sqrt{\sum_{i=1}^{n}(O_i - \bar{O})^2}} \right)^2 \tag{15}$$

$$\text{RMSE} = \sqrt{\sum_{i=1}^{n} \frac{(E_i - O_i)^2}{n}} \tag{16}$$

$$\text{BIAS} = \frac{\sum_{i=1}^{n}(E_i - O_i)}{n} \tag{17}$$

$$\text{MAPD} = \frac{100}{n} \sum_{i=1}^{n} \left| \frac{E_i - O_i}{O_i} \right| \tag{18}$$

$$\text{KGE} = 1 - \sqrt{(r-1)^2 + \left(\frac{\sigma_E}{\sigma_o} - 1\right)^2 + \left(\frac{\bar{E}}{\bar{O}} - 1\right)^2} \tag{19}$$

454   Where R^2 is the coefficient of determination, RMSE is root-mean-square error, BIAS is the mean

455   bias, MAPD is the mean absolute percent deviation, KGE is Kling-Gupta efficiency, n is the total

456   number of data pairs, the bar indicates mean value of the measured variable and model estimates

457   of the same variable. E_i and O_i are the model estimated and measured SEB fluxes, r is the Pearson's

458   correlation coefficient and $\bar{O}$ is the average of measured values and $\bar{E}$ is the average of estimated

459 values and σ_o is standard deviation of observation values and σ_E is the standard deviation of

460 estimated values. The KGE has been widely used for calibration and evaluation hydrological

461 models in recent years and it combines the three components of Nash-Sutcliffe efficiency (NSE)

462 of model errors (i.e., correlation, bias, ratio of variances or coefficients of variation) in a more

463 balanced way. But it has not been widely used for analyzing the ET model performances. KGE = 1

464 indicates perfect agreement between modeled estimates and observations. The performance of a

465 model is considered 'poor' for KGE between 0 and 0.5 and models with negative KGE values is

466 considered 'not satisfactory'.

467 **4 Results**

468 **4.1 Ecosystem- scale surface soil temperature amplitude (A)**

469 The scaling functions developed to estimate ecosystem-scale (1km) surface soil temperature

470 amplitude (A) from point-scale T_{STA} were used to estimate G_i. However, before the development

471 of the scaling functions, analysis was carried out to investigate the relationship of soil temperature

472 amplitude between the two different spatial scales. The scatterplot (Fig. 5a) of noon-night LST

473 difference (ΔTs) versus T_{STA} for different albedo classes showed a linear increase in ΔTs with

474 increasing T_{STA}. However, some divergence of data points within the cluster were also noticed

475 which could be associated with different albedo (α_R) levels. Bivariate linear function was fitted

476 between T_{STA} as predictand (Y) versus ΔTs ($T_{sd} - T_{sn}$) and α_R as predictors (X1 and X2,

477 respectively). The function was found to be $Y = 0.59X1 - 51.3X2 + 8.66$ by combining the data

478 of nine ecosystems (r = 0.86). The coefficients in the above expressions correspond to B1 (0.59),

479 B2 (51.3), B3 (8.66) of eq. 5 in section 3.1.1.1. The estimated amplitude from this ecosystem-scale

480 predictors and scaling functions was treated as ecosystem-scale surface soil temperature amplitude

481 (A).
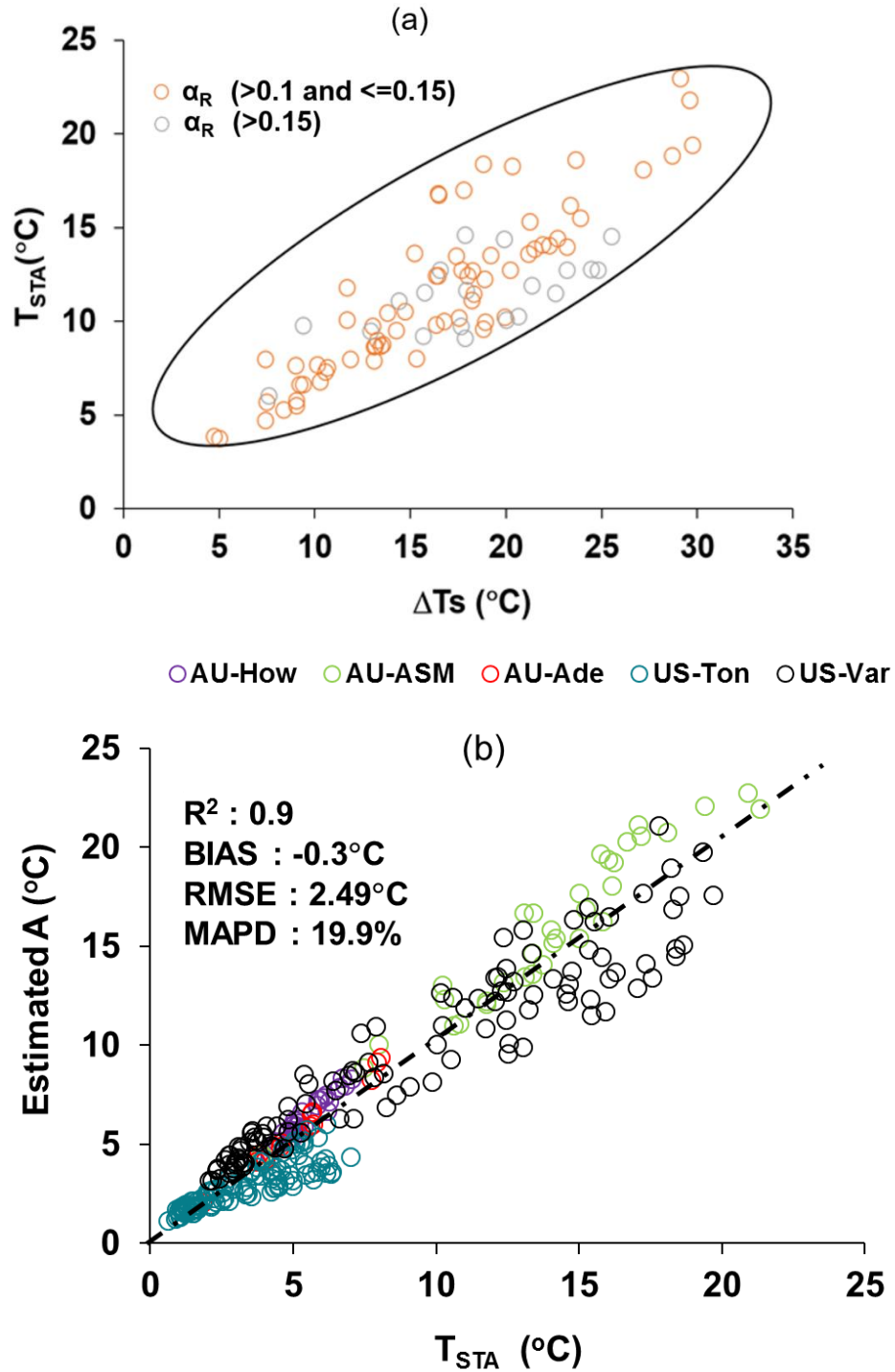
Figure 5. (a) Two-dimensional scatterplots between (ΔTs) versus T_{STA} at different α_R levels over different ecosystems. Here T_{STA} in y-axis is the observed soil temperature amplitude that is used to develop the scaling function and delta ΔTs is noon-night LST difference of MODIS AQUA; (b) Validation of ecosystem-scale estimates of A from the above functions over different sites.

482   Validation of ecosystem-scale estimates of A from the above functions over different sites is
483   shown in Fig. 5b with respect to T_{STA} for the independent datasets. The estimated A was found to
484   have MAPD of 19.9%, negative bias, and $R^2 = 0.90$ over different ecosystems. The temporal
485   variation of estimated A and T_{STA} is shown in Fig D1 in Appendix D. Further analysis was carried
486   out to investigate the bias in A at three fractional vegetation cover (f_c) classes ($f_c < 0.3$; $0.3 \leq f \; f_c$
487   ≤ 0.5; $f_c > 0.5$) representing bare soil (class 1), 30 – 50% canopy cover (class 2) and more than 50%
488   canopy cover (class 3), respectively. While negative bias was noted for class 1 and class 3 (-0.54°C
489   and -0.83° C), the bias was positive (0.49° C) in the intermediate f_c which represents sparse and
490   patchy canopy cover. The signals of surface albedo, emissivity and temperatures of soil surface
491   and canopy are relatively pure in class 1 and class 3 as compared to class 2, where the surface
492   signal carries more heterogeneity. Given T_{STA} is computed from the in-situ measurements, it is
493   likely to carry more heterogeneity in class 2 as compared to the other two classes. The land surface
494   emissivity in MYD11A2 was estimated from land cover types and anisotropy factor, which have
495   differential impacts on T_{ST} and T_S leading to such opposite bias in class 2 as compared to class 1
496   and class 3.

497   **4.2 Sensitivity analysis of STIC-TI G_i, LE_i and H_i to land surface variables**

498   **4.2.1 Sensitivity of G_i to land surface variables**

499   The average sensitivity of G_i to three land surface variables (T_S, NDVI, α_R) by combining the
500   estimates of wet and dry periods is shown in Fig. 6. G_i was found to be substantially sensitive to
501   T_S with error magnitude ranging from 2 – 18% due to T_S uncertainties of ±0.5 – 2.5 K (Fig. 6a),
502   with greater sensitivity to T_S during the summer season. The median sensitivity of G_i due to ±5 –
503   10% uncertainty in α_R varied from 5 to 12% in all the ecosystems (Fig. 6b). The uncertainties in
504   NDVI revealed 2 to 15% error in G_i estimates (Fig. 6c), and no significant difference in the mean
505   sensitivity due to NDVI uncertainties was noted between the ecosystems. The sensitivity of G_i
506   decreased with increasing values of NDVI.

507   **4.2.2 Sensitivity of LE_i and H_i to land surface variables**

508   Both LE_i and H_i were sensitive to T_S to the order of 2 – 29% (LE_i) and 5 – 35% (H_i) for T_S
509   uncertainty of ±0.5 – 2.5 K from its mean values (Table 3). Interestingly, LE_i was more sensitive
510   to T_S uncertainties as compared to H_i in the rainfed ecosystems. The highest mean sensitivity of

LE$_i$ to T$_S$ was found in arid (IND-Jai: 2 – 28%), semi-arid (AU-ASM: 5 – 21%), tropical savanna (IND-Dha: 3 – 26%), savanna (US-Ton: 4-29%) and arid (US-Var: 3-26%) ecosystems. The mean sensitivity of H$_i$ to T$_S$ was maximum in sub-humid (IND-Sam: 2 – 32%), semi-arid (IND-Naw: 2 – 28%), savanna (AU-Ade: 8 – 17%) (Table 3). A greater sensitivity of the SEB fluxes due to α_R uncertainties was found than due to NDVI. The median sensitivity of LE$_i$ and H$_i$ due to 10% uncertainty from mean α_R varied within 2 – 16% in all the ecosystems (Table 3). By contrast, errors in the two SEB fluxes were substantially low (2 – 13%) due to ±0.05 – 0.15 uncertainty from mean NDVI (Table 3).
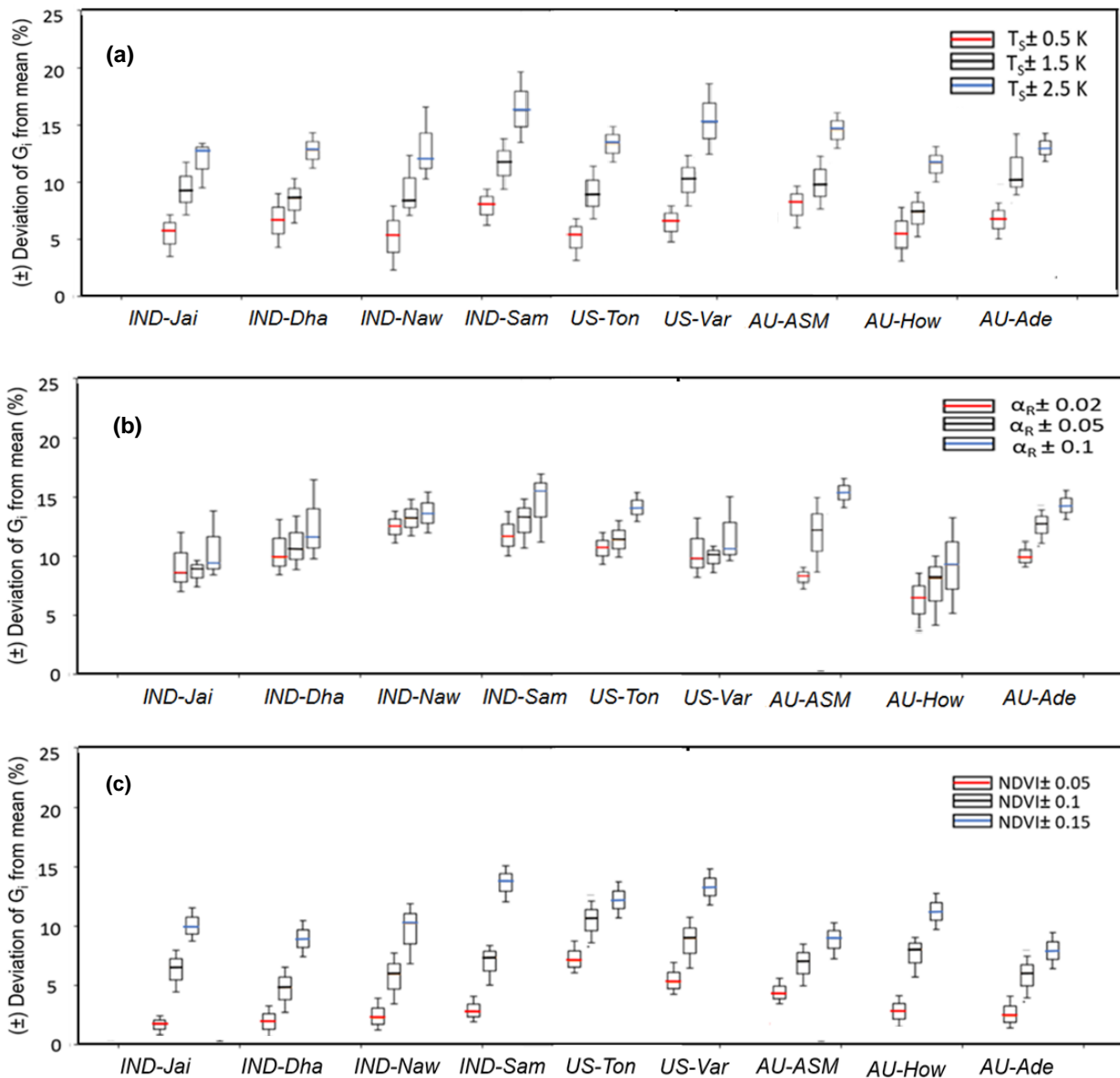
Figure 6: Sensitivity of STIC-TI G_i due to uncertainties in T_S (a), α_R (b), and NDVI (c) for eight flux tower sites in India and Australia. The uncertainties were introduced by taking the mean values of these variables during three different periods (summer, rainy and winter) of a year. Mean uncertainties of the three periods are presented in the figure.

519 **Table 3:** Sensitivity (in percent) of LE_i and H_i due to T_S, NDVI, and α_R uncertainties

| Study sites | Sensitivity of LE_i and H_i to T_S, NDVI and α_R (percent change) | | | | | |
| | T_S uncertainty ($\pm0.5 - 2.5$ K) | | α_R uncertainty ($\pm5 - 10\%$) | | NDVI uncertainty ($\pm0.05 - 0.15$) | |
	LE_i	H_i	LE_i	H_i	LE_i	H_i
IND-Jai	2-28	1-6	3-14	2-13	2-8	2-6
IND-Dha	3-26	2-8	2-12	3-12	3-10	3-9
IND-Naw	1-20	2-28	2-10	3-10	2-7	2-6
IND-Sam	1-16	5-32	4-13	6-11	2-5	2-7
US-Ton	4-29	4-12	3-12	4-12	3-8	5-7
US-Var	3-26	6-14	4-11	2-10	4-10	2-8
AU-ASM	5-21	2-10	3-12	2-13	2-10	2-11
AU-How	8-13	2-15	2-11	4-16	3-12	3-13
AU-Ade	2-17	8-17	3-12	2-10	3-10	3-9

520 **4.3 Comparative evaluation of STIC-TI and contemporary G_i models**

521 The performances of STIC-TI and existing G_i models were evaluated and compared with respect

522 to *in-situ* G_i measurements. The existing models reported by Moran et al. (1989), Bastiaanssen et

523 al. (1998), Su (2002), and Boegh et al. (2004) have been considered for comparing with TI-based

524 model. These four existing models are referred here as MOR89, BAS98, SU02 and BO04,

525 respectively. While the models MOR89, SU02 and BO04 are based on linear regression between

526 G versus NDVI, BAS98 is based on multivariate regression of G with NDVI, LST and α_R. The

527 performance of the STIC-TI was substantially better as compared to MOR89, SU02 and BO04

528 with respect to MAPD (19%), RMSE (22 Wm^{-2}) and coefficient of determination ($R^2 = 0.8$) when

529 compared with *in-situ* measurements over one Indian, three Australian and two US flux tower sites

530　(Table 4) and comparable with BAS98 G_i model. The validation plot of retrieved noontime Gi

531　from STIC-TI is shown in Fig. 7.
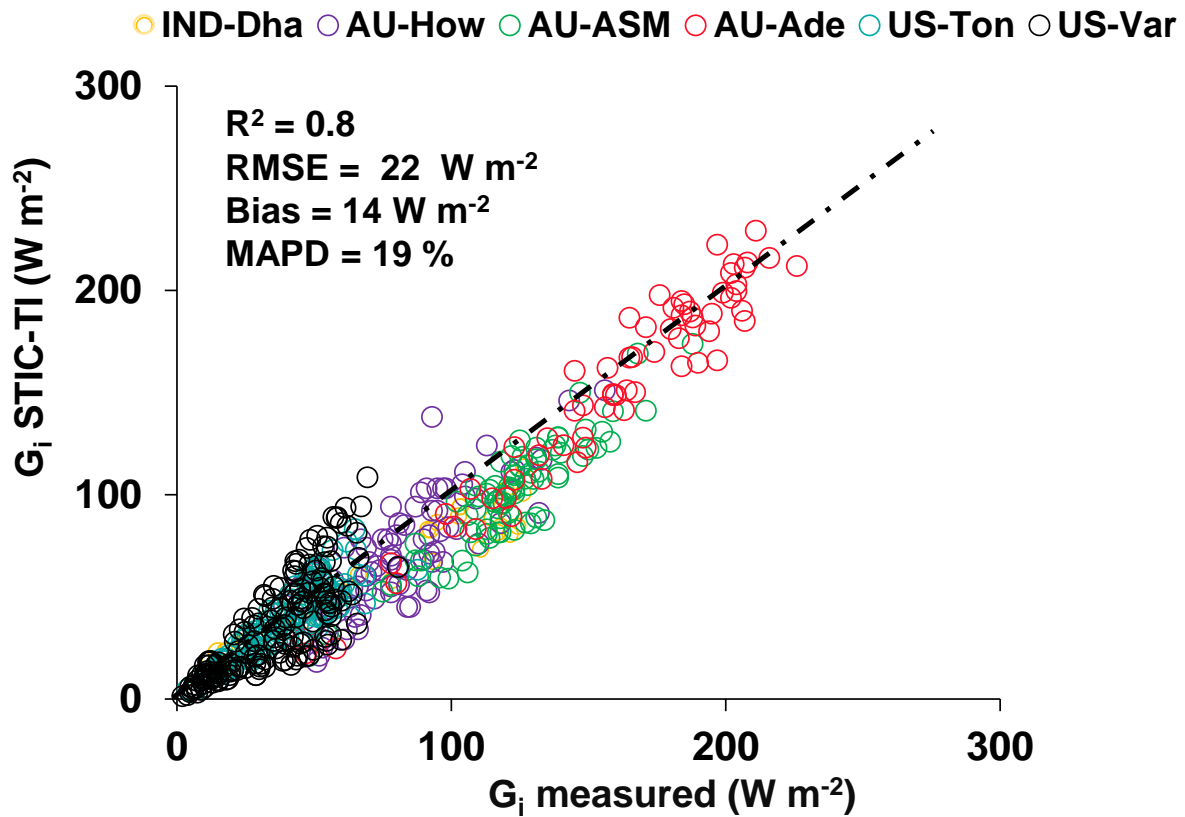
Figure 7: Validation of noontime (1:30 pm) G_i estimates with respect to in-situ measurements in different ecosystems. The regression between the two sources of G_i is G_i (STIC-TI) = 0.90G_i (tower) -0.10.

532　**Table 4**: A comparison of error statistics of G_i estimates from STIC-TI and existing G_i models
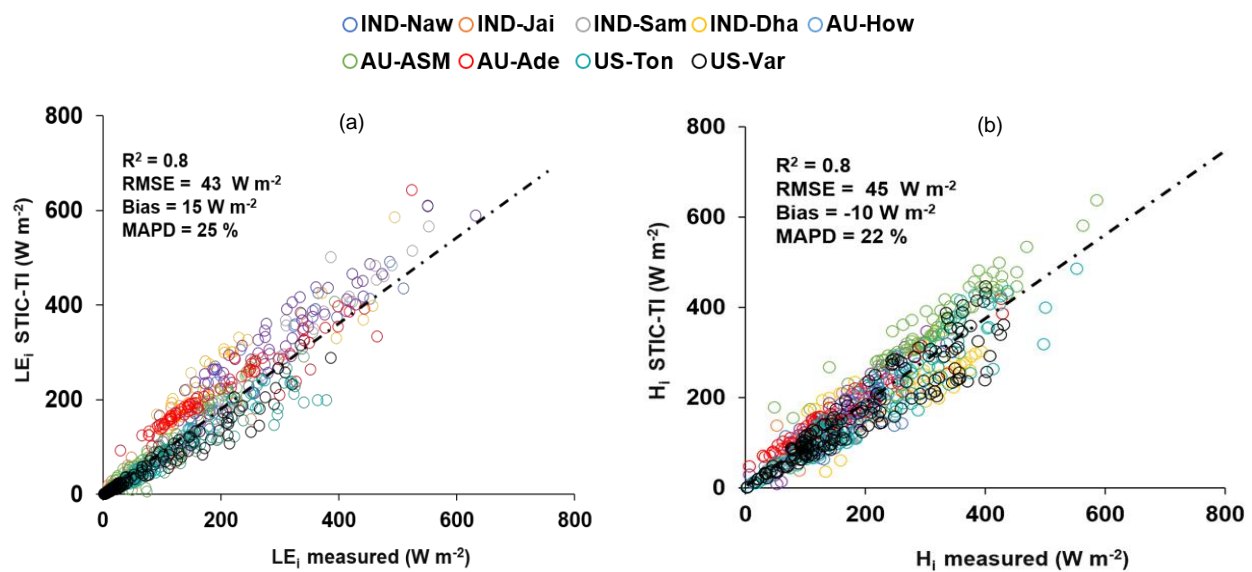
533　over different ecosystems

G models	R^2	RMSE (W m^{-2})	MAPD (%)	KGE
STIC-TI	0.80	22	19	0.74
MOR89	0.70	31	29	0.46
BAS98	0.80	20	18	0.61
SU02	0.80	30	26	0.54
BO04	0.70	35	29	0.48

534　The RMSE varied from 9 to 20 W m^{-2} with MAPD ranging from 12 to 21% across individual flux

535　tower sites. High magnitude of G_i was predicted in the arid and semi-arid systems (120 – 240 W

536   m^{-2}) as compared to the humid systems (20 – 90 W m^{-2}), which was in close correspondence with

537   the observations. The model also captured the range of G_i that are generally found in different

538   biomes (20 – 140 W m^{-2} for grasslands, 20 – 90 W m^{-2} for cropland) (Purdy et al., 2016). Due to

539   the paucity of G_i measurements, direct validation of G_i was only possible for 32 days (concurrent

540   to MODIS overpass) at the IND-Dha site. Overall, STIC-TI tends to provide reasonable G

541   estimates for the terrestrial ecosystems having soil temperature amplitude above 5ºC.

542   **4.4 Evaluation of STIC-TI LE_i, H_i, and EF**

543   The modeled versus measured LE_i and H_i showed good agreement in all the nine ecosystems with

544   RMSE in LE_i and H_i estimates using MYD11 LST product to the order of 29 – 62 W m^{-2} and 26 –

545   61 W m^{-2}, MAPD of 9 – 31% and 20 – 36%, BIAS of -29 to 38 W m^{-2} and -44 to 32 W m^{-2} (Fig.

546   8a, b; Table 5) and high R^2 of 0.8.

Figure 8: (a) Validation of STIC-TI LE_i estimates with respect to *in-situ* measurements in different ecosystems; (b) Validation of STIC-TI H_i estimates with respect to *in-situ* measurements in different ecosystems.

547

548   **Table 5**: Error statistics of STIC-TI LE_i and H_i estimates with respect to EC measurements in

549   different ecosystems of India, US, and Australia using MYD11A2 LST product for all nine sites

550   and using MYD21A2 LST product for three semi-arid and arid sites. The statistics obtained by

551   using MYD21A2LST are shown in the parentheses.

552

Sites	STIC-TI (LE_i and H_i)									
	R^2		BIAS (W m^{-2})		RMSE (W m^{-2})		MAPD (%)		KGE	
	LE_i	H_i	LE_i	H_i	LE_i	H_i	LE_i	H_i	LE_i	H_i
IND-Jai	0.90 (0.91)	0.90 (0.92)	-21 (-16)	12 (9)	57 (45)	27 (21)	31 (24)	22 (19)	0.80 (0.82)	0.76 (0.79)
IND-Naw	0.90 (0.92)	0.80 (0.85)	19 (12)	-26 (-16)	44 (37)	51 (46)	17 (16)	28 (25)	0.92 (0.92)	0.71 (0.73)
IND-Dha	0.90	0.90	38	-44	43	35	27	25	0.71	0.64
IND-Sam	0.90	0.80	12	-10	32	61	9	27	0.95	0.70
US-Ton	0.90 (0.91)	0.90 (0.92)	-29 (-18)	-32 (-21)	53 (45)	34 (27)	25 (22)	17 (15)	0.85 (0.87)	0.91 (0.93)
US-Var	0.90	0.80	-19	-28	49	39	27	20	0.82	0.89
AU-ASM	0.90 (0.93)	0.90 (0.91)	-3 (6)	22 (16)	46 (37)	26 (18)	29 (24)	20 (17)	0.94 (0.95)	0.83 (0.85)
AU-How	0.90	0.90	16	-25	42	27	17	21	0.89	0.85
AU-Ade	0.90	0.90	21	15	29	53	28	36	0.77	0.80

553

Arid ecosystems in India (IND-Jai), US (Ton and Var) and semi-arid ecosystem in Australia (AU-ASM) revealed relatively high MAPD (31%, 25%, 27%, and 28%) (Table 5). In general, STIC-TI was able to produce the dominant convective heat fluxes with respect to the EC measurements as evident through low RMSE for H_i and high RMSE for LE_i in the IND-Jai, US-Ton, US-Var, and AU-Ade where LE_i is inherently low except few rainy days. A uniform distribution of data points around 1:1 validation line (Fig. 8a) indicated overall low BIAS in LE_i estimates. However, modeled H_i was consistently lower than the observations (negative BIAS) in the tropical savanna (IND-Dha and AU-How) and semi-arid (IND-Naw) ecosystems [(-44) – (-25) W m^{-2} and -26 W m^{-2}) while a consistent positive BIAS was observed in the AU-ASM (semi-arid) and AU-Ade (savanna), US-Var (arid) (Fig. 8b; Table 5). This consequently led to overall low negative BIAS (-10 W m^{-2}), relatively low R^2 in H_i ($R^2 = 0.8$) as compared to the errors in LE_i (BIAS = 15 W m^{-2}, $R^2 = 0.9$). The regression between the modeled and tower measurements of LE_i is LE_i(STIC-TI) = 0.98LE_i(tower) – 0.266. The regression between the modeled and tower measurements of H_i is H_i (STIC-TI) = 0.93H_i(tower) + 4.90. The KGE statistics varied in the range of 0.71 – 0.95 for LE_i and in the range of 0.64 – 0.91 for H_i, respectively across all nine flux tower sites, thus revealed reasonably high efficiency of the model to capture the magnitude and variability of SEB fluxes.

570   The impact of MODIS Aqua day-night view angle difference (δVZA) on STIC-TI fluxes was

571   further investigated. Estimated errors in terms of mean percent deviation in LE_i, H_i and G_i with

572   respect to measurements for each 10° bin over 16 angular bins within ±80° were analysed in

573   response to mean δVZA of each angular bin. G_i errors (X) were found to be significantly correlated

574   with δVZA (Y) in a parabolic (Y = $0.0027X^2$ − 0.0025X + 1.4919; r = 0.73) pattern (Refer

575   Appendix F, Figure F1(a)). Errors in G_i to the order of-5 to 10%, 10-15% and >15% were largely

576   found to be within ±30°, ±45°, and >45° to -80° δVZA, respectively. The errors in H_i were found

577   to have strong linear (Y = -0.1452X + 1.1146, r = 0.77) dependence on δVZA (Refer Appendix F,

578   Figure F1(b)). However, a weak dependence of LE_i errors (Y = -0.0878X + 2.0314, r = 0.5) on

579   δVZA (Refer Appendix F, Figure F1(c)) was found, as majority of the errors were within ±10%

580   that corresponded to ±60° δVZA. The nature of relations and degree of dependency of model flux

581   errors on δVZA in this study would be helpful to minimize the error budget in surface energy

582   balance fluxes from future thermal infrared missions having day-night observations.
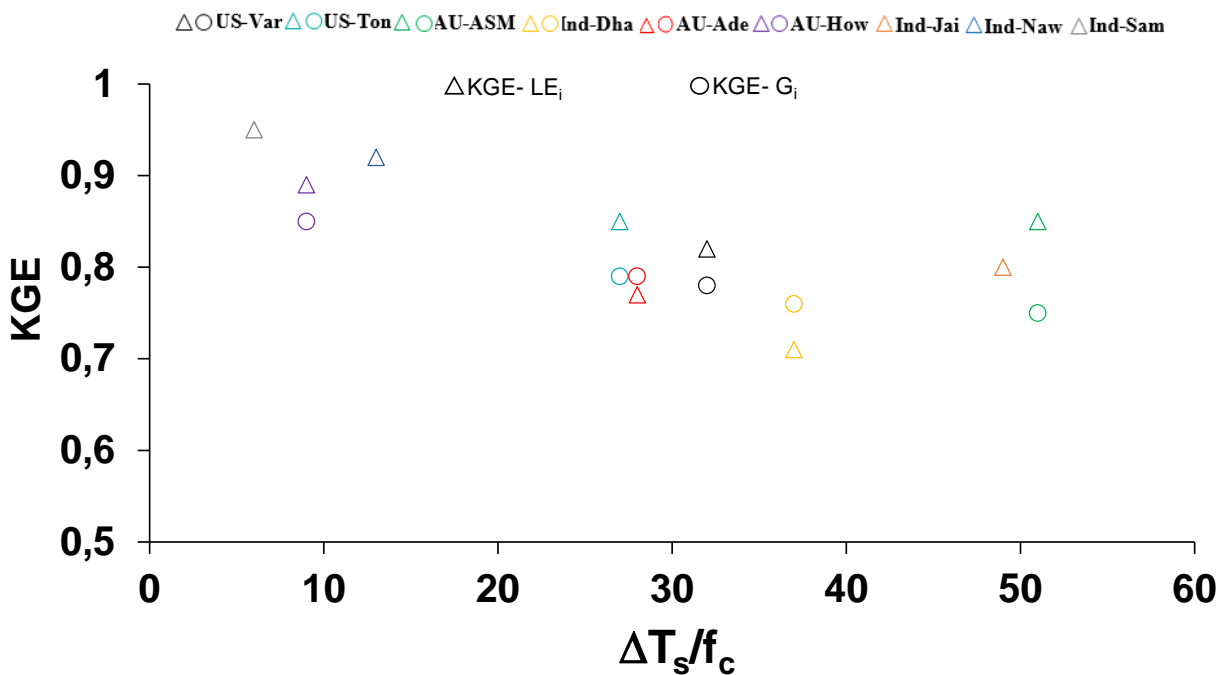
Figure 9: Relationship between KGE of STIC-TI (G_i and LE_i) with $\Delta T_s/f_c$ in different terrestrial ecosystems.

583   Further investigation was made on whether KGE for STIC-TI G_i and LE_i follow any systematic

584   pattern and the ratio ΔT_S and f_c was used as proxy for surface heterogeneity and dryness. The plot

585   of KGE of G_i and LE_i with this ratio is shown in Fig. 9. KGE-G_i was found to show a systematic

586   decrease with increase in ΔTs-fc ratio up to 40, after which it remained unchanged with increase

587   in the ratio. Although KGE of LE_i also decreased (20% reduction) with increase in ΔTs-f_c ratio,

588   KGE-LE_i was found to increase beyond ΔTs-f_c 40. This revealed that the model efficiency

589   remained high (>0.8) within certain dryness limits (ΔTs-f_c ratio <20 and >50) and the efficiency

590   reduced moderately (within 0.7 – 0.8) for intermediate dryness. Interestingly, the use of

591   MYD21A2 LST in STIC-TI showed improvements (see the parentheses in different columns in

592   Table 5) in LE_i and H_i error statistics as compared to using MYD11A2 LST in terms of higher R^2

593   and KGE, and lower RMSE in LE_i (3-8% less) and H_i (2-3% less) for semi-arid and arid sites such

594   as IND-Jai, IND-Naw and US-Ton.

595   An independent evaluation of multi-temporal heat fluxes over two US flux sites for the years 2016-

596   2018 is shown in Fig. 10 and Fig 11. STIC-TI G_i estimates with MYD11A2 LST product showed

597   close match with *in-situ* measurements with respect to intra and inter-annual variability in G_i

598   followed by LE_i and H_i. This further demonstrates the merit of the coupled model for reproducing

599   ecosystem-scale G_i estimates especially for shorter and open canopies.
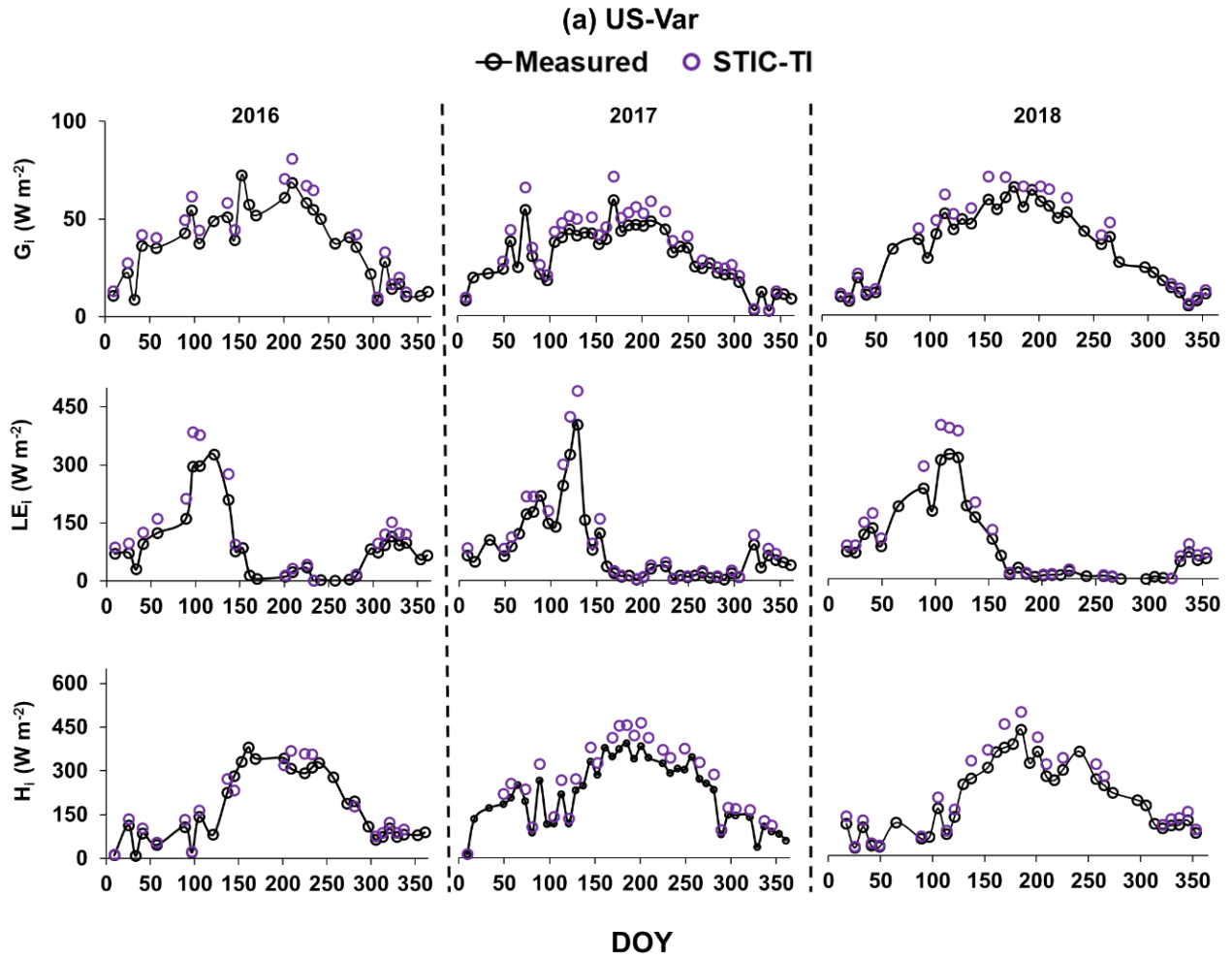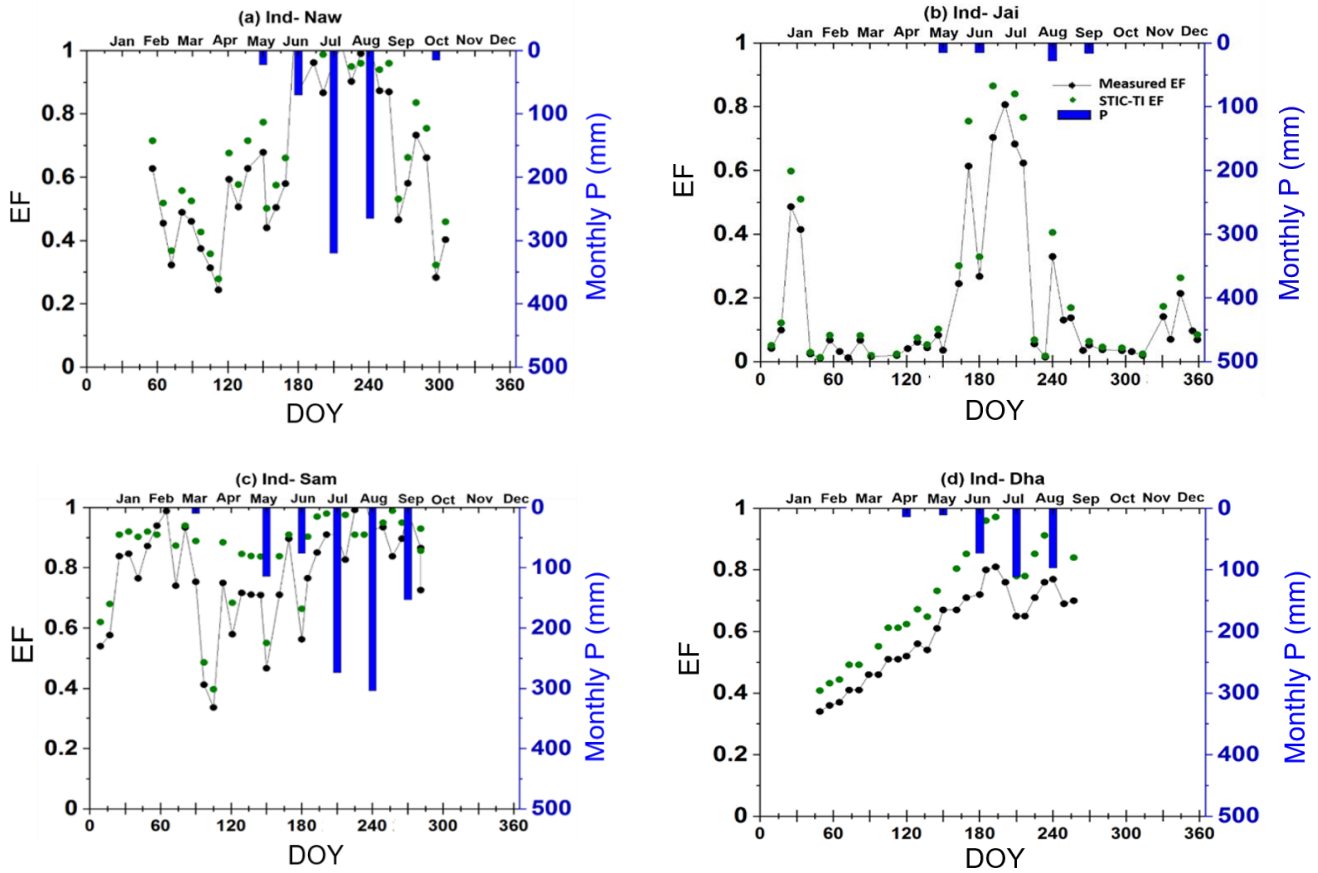
Figure 10: Illustrative examples of temporal evolution of STIC-TI derived fluxes using MYD11A2 LST product versus observed SEB fluxes for three consecutive years from 2016 to 2018 in a grassland ecosystem in United States (e.g., US-Var).
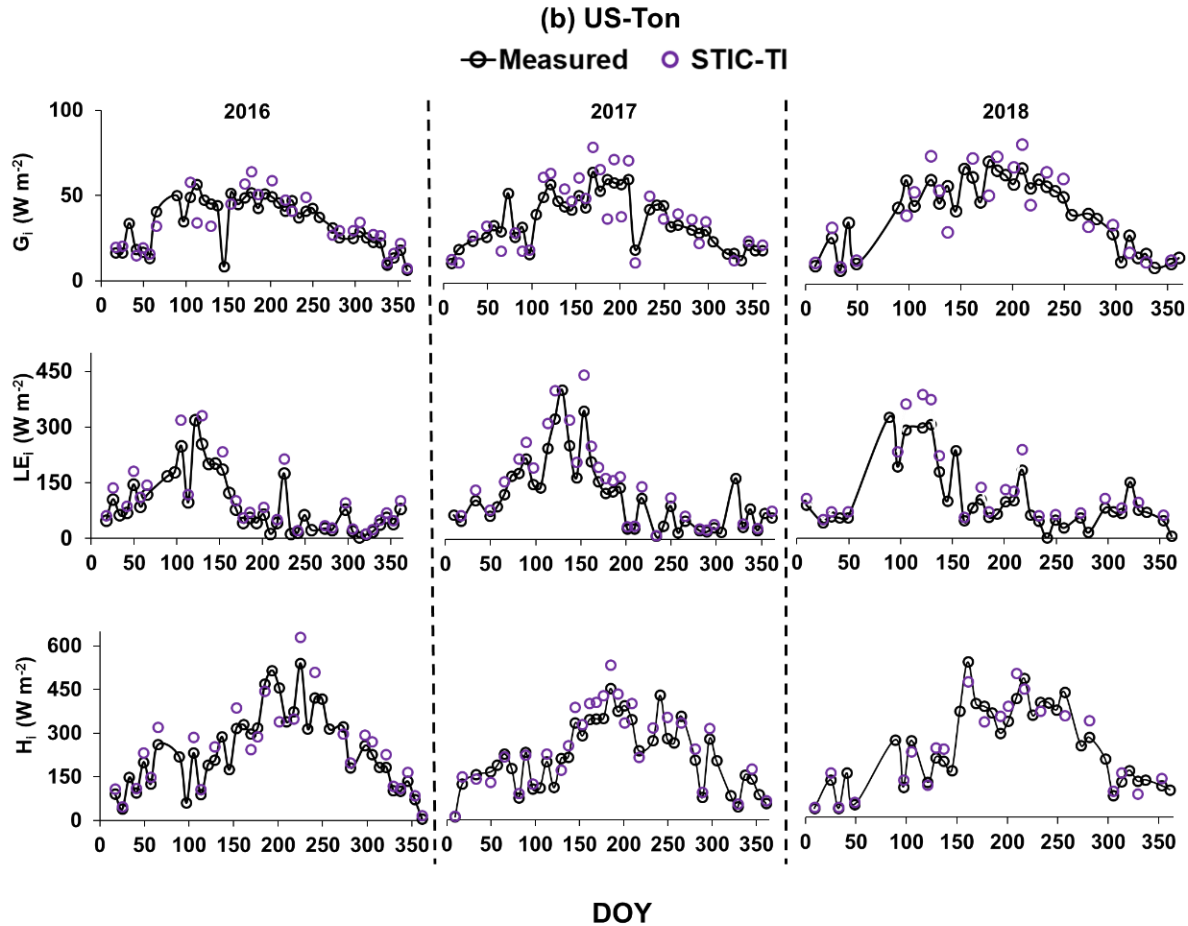
Figure 11: Illustrative examples of temporal evolution of STIC-TI derived fluxes using MYD11A2 LST product versus observed SEB fluxes for three consecutive years from 2016 to 2018 in a woody savanna ecosystem in the United States (e.g., US-Ton).

600   The temporal behavior of STIC-TI and observed evaporative fraction (EF) (ratio of LE and R_N –

601   G) (Fig. 12) along with observed monthly rainfall (P) distinctly captured the substantial temporal

602   variability in EF during the dry-to-wet transition in the Indian study sites, which also corresponded

603   to low (high) θ and P. In IND-Naw and IND-Sam, a marked rise (>0.4) in STIC-TI EF was noted

604   during day-of-the-year (DOY) 25 to 75 where wheat is grown under assured irrigation. The impact

605   of irrigation is thus captured by the substantial increase in EF in the absence of P. In contrast, the

606   rainfed grassland system (IND-Jai) showed peak EF (~0.8), which corresponded to south-west

607   monsoon rainfall during June to September and a progressive decline in EF during the dry down

608   period in October to April corresponding to post south-west monsoon phase. Some intermittent

609   spikes in EF were also noted during dry-down phase in both STIC-TI and observations. The

610   intermittent EF spikes during the soil moisture dry down phase could be due to enhanced LE

34

611   through moisture advection from the surrounding vegetation causing an enhancement of
612   evaporation than expected. This is known as the 'clothesline effect' which frequently occurs in
613   semi-arid and arid ecosystems. In addition to IND-Jai, the response of both modeled and measured
614   EF to wet and dry spells was also noted during south-west monsoon period at all other flux tower
615   sites of India.

Figure 12: Illustrative examples of temporal variation of STIC-TI derived EF using MYD11A2 LST product with respect to measured EF and P in (a) IND-Naw, (b) IND-Jai, (c) IND-Sam, and (d) IND-Dha

616   The temporal behavior of EF from STIC-TI using MYD11A2 LST product and EC measurements
617   along with measured θ and P at the OzFlux and AmeriFlux sites also revealed (Fig. 13) close
618   correspondence of STIC-TI with EC observations. Low EF (0.05 – 0.40) during the dry season
619   around DOY 100 – 250 and high EF (>0.4) during the wet season (DOY 1 – 120 and 300 to 360)
620   in AU-ASM, US-Ton and US-Var was observed. The analysis showed that STIC-TI EF can
621   capture the annual variability of observed EF and its responses across different ecosystems during
622   wet and dry seasons. The plots of STIC-TI EF versus measured θ (in the inset of Fig. 13) revealed

623　triangular scatter close to right-angled triangle with positive slope of hypotenuse in three

624　ecosystems AU-ASM, US-Var and US-Ton. This showed that in the water-controlled ecosystems,

625　where distinct wet-dry seasons exist, the positive EF-θ relationship is an outcome of the soil

626　moisture controls on transpiration during the dry season.
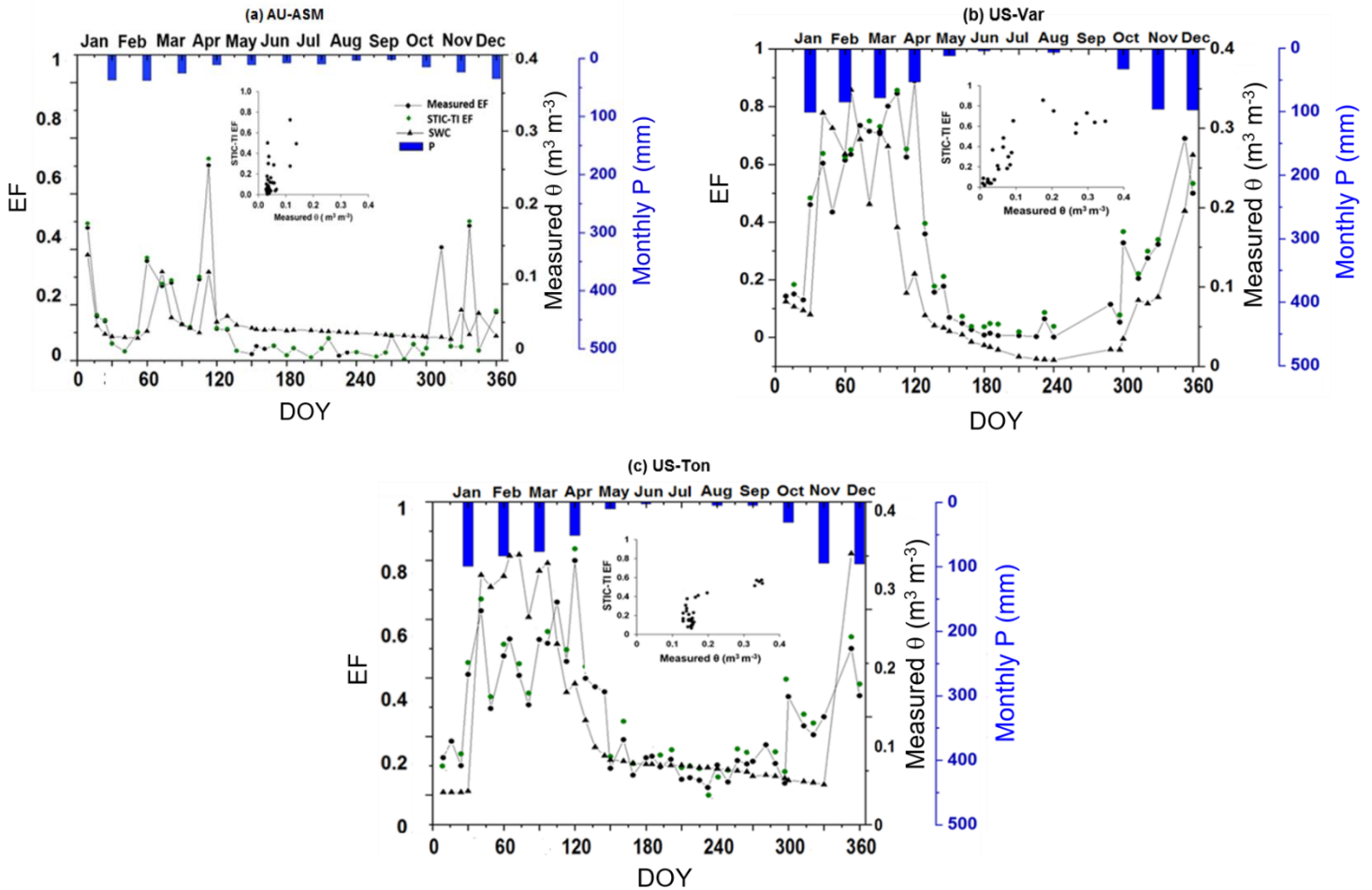
Figure 13: Comparison of temporal variation of STIC-TI derived EF using MYD11A2 LST with respect to measured EF, θ and Pin (a) AU-ASM, (b) US-Var, (c) US-Ton. The scatterplots in the inset shows the relationship between STIC-TI EF with respect to measured θ.

627　**5 Discussion**

628　**5.1 Interaction of flux and internal SEB metrices**

629　From section 4.1 we found relatively reduced sensitivity of G_i to Ts uncertainties. In any given

630　condition, if an over(under) estimation of M due to noontime T_S uncertainties (through eq. 13)

631　leads to an over(under) estimation of Γ, the effects of such over(under) estimation of Γ(due to

632   noontime T_S uncertainties) tend to be compensated by under(over) estimation of amplitude A (in

633   eq. 5), ultimately leading to a reduction of the sensitivity of G_i to T_S. While the scatter between G

634   versus A for a wide range of Γ (Fig. 14a) revealed large scatter with increasing amplitude under

635   the dry conditions (low Γ), the scatter between Γ versus T_S for different M (Fig. 14b) revealed

636   exponential reduction of Γ with increasing Ts and dryness, and almost no significant change in Γ

637   with increasing T_S at a constantly high dryness (M<0.25). Thus, the confounding effects of Γ, A,

638   and M through eq. 3, 5, 12 and 13 led to a reduction of sensitivity of G to T_S, as exemplified in

639   Fig. 14.

(a)   (b)
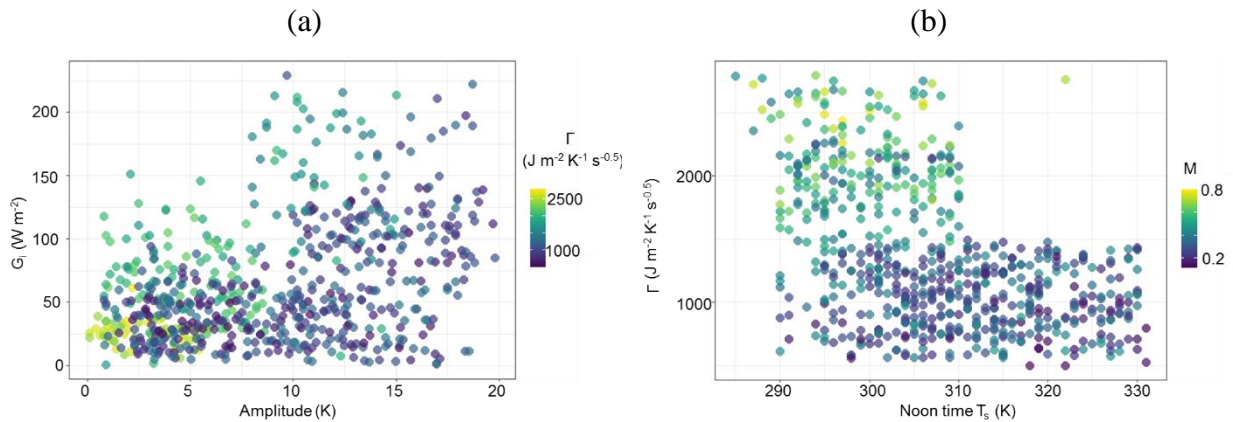
Figure 14: Response plots among parameters of TI-based G_i model, such as (a) G_i versus Amplitude (A) for varying Γ, and (b) Noon-time T_S versus Γ with varying M.

640

641   Concerning LE_i and H_i, dual uncertainties could be propagated in both the fluxes through

642   daytime T_S (through M and G_i), leading to high sensitivity of these two SEB fluxes due to T_S

643   perturbations. The relatively high sensitivity of LE_i to T_S (as compared to H_i) in the non-

644   irrigated ecosystems could be due to partial compensation of g_A/g_S in both numerator and

645   denominator of the PMEB equation for H (eq. C7 of Appendix C). A recent study (Fig.10 in

646   Mallick et al., 2018a) showed high sensitivity of g_S due to T_S (1% change in T_S led to 5.2–7.5%

647   change in g_S) as compared to g_A sensitivity to T_S (1% change in T_S led to 1.6–2% change in g_A),

648   suggesting that errors in g_S due to T_S uncertainty tend to be larger than errors in g_A. Partial

649   cancellation of the conductance errors in the numerator of eq. (C7 of Appendix C) might have

650   resulted in compensation of H_i errors in the water-limited ecosystems. In this environment, the

651   variability of LE_i is mainly dominated by g_A/g_S, which makes LE_i highly sensitive due to T_S

652   uncertainties. Combined uncertainty due to g_A/g_S in the denominator and g_A in the numerator

653   of eq. (C6 of Appendix C) resulted into greater sensitivity in LE_i to T_S in the arid and tropical

654   savannah ecosystems (Mallick et al., 2015, 2018a; Winter & Eltahir, 2010). The very low

655   sensitivity of LE_i and Hi due to uncertainties in NDVI is because NDVI was not used in the

656   conductance parameterizations and effects due to NDVI in STIC-TI was only propagated

657   through G_i. The sensitivity of LE_i and H_i to albedo was mainly due to the dependence of net

658   radiation (R_{Ni}) on albedo, and any resultant uncertainty in R_{Ni} (due to albedo) tends to be

659   reflected in the sensitivity of LE_i and H_i to albedo.

5.2 Possible sources of errors in SEB flux evaluation

661   In STIC-TI, underestimation and overestimation errors in G_i in different ecosystems (Fig. 7) could

662   originate due to the errors in MYD11A2 LST product. A host of studies previously reported that

663   the standard deviations of errors in retrieved emissivity in bands 31 and 32 are 0.009, and the

664   maximum error in retrieved Ts of MOD11A1 LST falls within 2-3 K, which is mainly due to the

665   errors in surface emissivity correction (Duan et al., 2017; Wan, 2014; Lei et al., 2018). In the

666   present analysis, we found an overestimation error of MODIS T_S in the range of 0.5 – 1.5 K when

667   compared with *in-situ* infrared temperature measurements at the tropical savanna site. As

668   mentioned in section 3.1, a positive (negative) bias in T_S would tend to an overestimation

669   (underestimation) of amplitude (A) in eq. (5); underestimation (overestimation) of M in eq. (13),

670   and consequent underestimation (overestimation) of Γ (eq. 12) and G_i, respectively. Furthermore,

671   the standard deviation of NDVI surrounding the tower sites varied from 0.01 – 0.05 when

672   compared to the ground measurements, which could be another source of error in the STIC-TI

673   model. In addition, NDVI saturates at LAI > 3. However, STIC-TI provides direct estimates of

674   ecosystem G and is independent of R_N.

675   Despite the comparable accuracy of current G estimates with the G model of Bastiaanssen et al

676   (1998), the foundation of STIC-TI lies in the use of soil moisture characteristics with varying soil

677   textural types which are known to influence the soil heat conductance and thereby G. Thus, the

678   control of soil moisture on evaporation is explicitly included in STIC-TI as opposed to the semi-

679   empirical G function of Bastiaanssen et al (1998). The higher accuracies of TI-based thermal

680   diffusion model as compared to R_N-based empirical G models were also reported by Purdy et al.

681   (2016) at daily or longer time scales in cropland, grassland. All these G model estimates many a

682   times differ from in situ measurements because of the no accounting of leaf litter presence or layer

683   on soil floor in the remote sensing-based G-model.

684   The overestimation (underestimation) of $LE_i(H_i)$ is also due to the effects of spatial resolution of

685   different input variables on these two SEB fluxes and conducted statistical evaluation with respect

686   to the measured SEB fluxes. Eswar et al. (2017) demonstrated the need for spatial disaggregation

687   models for monitoring LE_i at field scale using contextual models by disaggregation of evaporative

688   fraction (Λ) and downwelling shortwave radiation ratio (R_G). Using different disaggregation

689   models, they estimated LE_i at 250m spatial resolution and reported RMSE of $30 – 32$ W m^{-2} as

690   compared to LE_i obtained at 1000m spatial resolution with RMSE of $40 – 70$ Wm^{-2} over different

691   sites in India. Anderson et al. (2007) reviewed different validation experiments conducted in

692   diverse agricultural landscapes (Anderson et al.,2004, 2005; Norman et al., 2003) and reported

693   RMSE in LE_i in the range of $35 – 40$ W m^{-2} (15%) at $30 – 120$ m disaggregated spatial resolution.

694   Current analysis also brought out the need for noon-night thermal imaging with spatial resolution

695   finer than 1000m to adequately capture the magnitude and variability of LE_i in the terrestrial

696   ecosystems especially agroecosystems where average field sizes are less (< 0.5 ha) and fragmented

697   such as in India and other sub-continents.

698   As seen in Fig. 8a and Table 5, there is a gross overestimation of LE_i with respect to the tower

699   observations when MYD11A2 LST was used. The consistent positive BIAS in STIC-TI LE_i in

700   five out of nine sites is presumably due to the overestimation of R_{Ni} (Figure B1 of Appendix B)

701   and underestimation of G_i. Figure 7 shows overestimation of G_i for three OzFlux sites and US sites

702   and underestimation of G_i for Indian site with G_i (STIC-TI) = 0.90 G_i(tower) - 0.10 and

703   overestimation of R_{Ni} at the ecosystem-scale, with R_{Ni} (STIC-TI) = 0.78R_{Ni} (tower) +58.92

704   (Appendix-B2). This means a systematic overestimation of net available energy ($R_{Ni} – G_i$) will be

705   obvious in cases where STIC-TI shows underestimation of G_i. Since available energy is an

706   important component for estimating LE through the PMEB equation, an overestimation of net

707   available energy leads to an overestimation of LE by STIC-TI. Sensible heat flux will be

708   consequently underestimated due to the complementary nature of the PMEB equation. It may be

709   also noted that the use of MYD21A2 LST led to relatively better accuracy in LE_i (3-8%) and H_i

710   (2-3%) as compared to using MYD11A2 LST in semi-arid and arid ecosystems. The higher

711   retrieval accuracy of MYD21A2 LST using TES (Temperature-Emissivity Separation) algorithm

712   over MYD11A2 LST that uses split-window algorithm (Wan et al, 2015) is the main reason for

713   obtaining higher accuracy in LE_i and H_i estimates.

714   The standard deviations of MODIS Aqua day-night overpass time over study sites were found to

715   be within 30-45 minutes (Sharifnezhadazizi et al, 2019) and the expected deviation in LST from

716   the mean local time would be around $\pm0.75K$ (Sharifnezhadazizi et al, 2019). Sensitivity analysis

717   showed that resultant uncertainties in STIC-TI heat flux estimates would be of the order of ±5-7%

718   due to this LST uncertainty.

719   **5.3 Effects of SEB closure**

720   Given there is a widespread lack of SEB closure ($H + LE \neq R_N - G$) or residual energy balance,

721   knowledge of the impact of different vegetation types and climatic variables on SEB 'non-closure'

722   is essential. A recent study by Dare-Idowu et al. (2021) covering 8 growing seasons and 3 crops

723   (maize, wheat, and rapeseed) in two sites of south-western France showed that the systematic effect

724   of each site on SEB closure was stronger than the influence of crop type and stage. Same study

725   revealed a greater percentage of SEB closure under unstable atmospheric conditions and in the

726   prevailing wind directions, and sensible heat advection accounted for more than half of the

727   imbalance at both the sites.

728   In our study, using unclosed SEB observations for Indian sites in the absence of *in-situ* G_i

729   observations also added to the consistent positive BIAS in the statistical evaluation of LE_i. A

730   ubiquitous lack of energy balance closure to the order of $10 - 20\%$ worldwide at most of the EC

731   sites is reported in different literatures (Stoy et al., 2013; Wilson et al., 2002), which implies a

732   systematic underestimation (overestimation) of LE_i (EC tower) (and/or H_i(EC tower)).

733   Accommodating an average 15% imbalance in LE_i (EC tower) would tend to diminish the positive

734   BIAS in STIC-TI. Therefore, the pooled gain (0.98) and positive BIAS between the STIC-TI and

735   tower LE_i is determined by the overestimation of ($R_{Ni} - G_i$), combined with the underestimation

736   of measured LE_i from the EC towers. An underestimation of H_i (negative BIAS) is associated with

737   two reasons; (a) ignoring the two-sided aerodynamic conductance of the leaves (Jarvis and

738   McNaughton, 1986; Monteith and Unsworth, 2013; Schymanski et al., 2017), which could lead to

739   substantial underestimation of H_i, and (b) due to the complementary nature of the PMEB equation,

740   if LE_i is overestimated, H_i will be underestimated. In addition, frequent micro-advection fluxes

741   alter measured in situ H and LE fluxes. But these advection conditions are not explicitly accounted

742   in the current STIC-TI model. At the EC tower sites, the fraction of residual energy balance to R_N

743   can be quantified with respect to vegetation/crop growth characteristics or biophysical properties.

744   However, where G observations are lacking such as in many Indian EC tower sites, the TI-based

745   G model can be used to fill up the missing G observations to quantify residual energy balance and

746   to correct the SEB non-closure.

747   **6 Summary and conclusions**

748   This study addressed one of the long-term uncertainties in thermal remote sensing of evaporation

749   modeling in open canopy heterogeneous ecosystems, which is associated with empirical methods

750   of estimating ground heat flux. We demonstrated for the first-time physical integration and

751   coupling of a mechanistic ground heat flux model with an analytical evaporation model (Surface

752   Temperature Initiated Closure, STIC) within the surface energy balance equation. The model is

753   called STIC-TI, which uses satellite-based land surface temperature from MODIS Aqua and

754   associated biophysical variables, and it has minimal independence on *in-situ* measurements. The

755   estimation of evaporation through STIC-TI does not require any empirical function for inferring

756   the biophysical conductances. STIC-TI is independent of uncertain parameterizations of surface

757   roughness and atmospheric stability and does not also involve any look-up table for biome or plant

758   functional attributes. By linking noon-night land surface temperature with harmonics equation of

759   thermal inertia and soil moisture availability, STIC-TI derived the ground heat flux, and

760   subsequently coupled it with evaporation. Independent validation of STIC-TI with respect to eddy

761   covariance flux measurements from nine terrestrial ecosystems in arid, semi-arid and sub-humid

762   climate in India, USA and Australia led us to the following conclusions:

763   (i) While the MODIS Aqua day-night view angle difference showed strong impact on ground

764   heat flux and sensible heat flux estimate deviations of STIC-TI (with respect to

765   measurements), relatively weak dependence of latent heat flux errors on the day-night view

766   angle difference was noted.

767   (ii) The most notable advantages of STIC-TI are firstly, it provides direct estimates of ground heat

768   flux while simultaneously integrates the effects of soil water stress on ground heat flux and

769   evaporation through the inclusion noon-night land surface temperature information. Secondly,

41

770   the ecosystem-scale surface soil temperature amplitude used in the ground heat flux model

771   can advance our understanding on associated terrestrial ecosystem processes.

772   The requirement of few input variables in STIC-TI generates promise for surface-atmosphere

773   exchange studies using readily available data from the current generation remote sensing satellites

774   (e.g., MODIS, VIIRS) that have noon-night land surface temperature observations. STIC-TI can

775   also be potentially used for distributed ET mapping from future high spatial resolution (~ 50 – 60

776   m) TIR missions having noon-night observations with high revisit such as the Indo-French

777   mission, TRISHNA (**T**hermal infrared **I**maging **S**atellite for **H**igh-resolution **N**atural Resource

778   **A**ssessment) (Lagouarde et al., 2018, 2019), ESA's LSTM (Land Surface Temperature

779   Monitoring), and NASA SBG (Surface Biology and Geology), respectively.

780   **Author contributions**

781   KM and BKB conceptualized the idea; DD conducted STIC-TI model coding, simulations; BKB

782   and DD conducted the data analysis in consultation with KM; DD and BKB wrote the first version

783   of the manuscript with KM writing the introduction, discussions, and conclusions; BKB and KM

784   conducted all the analysis and writing during revision; all authors contributed to discussions,

785   editing and corrections; BKB and KM jointly finalized the manuscript.

Data and code availability

801 Harmonized time series datasets over the study grids are available in
802 https://doi.org/10.5281/zenodo.5806501. The model code is available to the first author upon
803 reasonable request.

References

805 Anderson, M., Kustas, W., Alfieri, J., Gao, F., Hain, C., Prueger, J., Evett, S., Colaizzi, P., Howell,
806   T. and Chávez, J.: Mapping daily evapotranspiration at Landsat spatial scales during the
807   BEAREX'08 field campaign, Adv. Water Resour., 50, 162 – 177,
808   https://doi.org/10.1016/j.advwatres.2012.06.005, 2012.

809 Anderson, M., Norman, J., Kustas, W., Li, F., Prueger, J. and Mecikalski, J.: Effects of Vegetation
810   Clumping on Two–Source Model Estimates of Surface Energy Fluxes from an Agricultural
811   Landscape during SMACEX, J. Hydrometeorol., 6(6), 892 – 909,
812   https://doi.org/10.1175/JHM465.1, 2005.

813 Anderson, M., Norman, J., Mecikalski, J., Otkin, J. and Kustas, W.: A climatological study of
814   evapotranspiration and moisture stress across the continental United States based on thermal
815   remote sensing: 1. Model formulation, J. Geophys. Res.: Atmos., 112(D10),
816   https://doi.org/10.1029/2006JD007506, 2007.

817 Anderson, M., Norman, J., Mecikalski, J., Torn, R., Kustas, W. and Basara, J.: A Multiscale
818   Remote Sensing Model for Disaggregating Regional Fluxes to Micrometeorological Scales, J.
819   Hydrometeorol., 5(2), 343 – 363, https://doi.org/10.1175/1525-
820   7541(2004)005<0343:AMRSMF>2.0.CO;2, 2004.

821 Bai, Y., Zhang, S., Bhattarai, N., Mallick, K., Liu, Q., Tang, L., Im, J., Guo, L., and Zhang, J: On
822   the use of machine learning based ensemble approaches to improve evapotranspiration
823   estimates from croplands across a wide environmental gradient, Agric. Forest Meteorol., 298
824   - 299, 108308, https://doi.org/10.1016/j.agrformet.2020.108308, 2021.

825 Bastiaanssen, W. G. M., Menenti, M., Feddes, R. A. and Holtslag, A. A. M.: A remote sensing
826   surface energy balance algorithm for land (SEBAL). 1. Formulation, J. Hydrol., 198 – 212,
827   doi:10.1016/S0022-1694(98)00253-4,1998.

828 Bennett, W., Wang, J. and Bras, R.: Estimation of Global Ground Heat Flux, J. Hydrometeorol.,
829   9(4), 744 – 759, https://doi.org/10.1175/2008JHM940.1, 2008.

830 Beringer, J., Hutley, L. B., McHugh, I., Arndt, S. K., Campbell, D., Cleugh, H. A., Cleverly, J.,
831   Resco de Dios, V., Eamus, D., Evans, B., Ewenz, C., Grace, P., Griebel, A., Haverd, V.,
832   Hinko-Najera, N., Huete, A., Isaac, P., Kanniah, K., Leuning, R., Liddell, M. J., Macfarlane,
833   C., Meyer, W., Moore, C., Pendall, E., Phillips, A., Phillips, R. L., Prober, S. M., Restrepo-
834   Coupe, N., Rutledge, S., Schroder, I., Silberstein, R., Southall, P., Yee, M. S., Tapper, N. J.,
835   van Gorsel, E., Vote, C., Walker, J., and Wardlaw, T.: An introduction to the Australian and
836   New Zealand flux tower network – OzFlux, Biogeosciences, 13, 5895–5916, doi:10.5194/bg-
837   13-5895-2016, 2016.

838 Bhat, G., Morrison, R., Taylor, C., Bhattacharya, B., Paleri, S., Desai, D., Evans, J., Pattnaik, S.,
839   Sekhar, M., Nigam, R., Sattar, A., Angadi, S., Kancha, D., Patidar, A., Tripathi, S., Krishnan,
840   K. and Sisodiya, A.: Spatial and temporal variability in energy and water vapor fluxes
841   observed at seven sites on the Indian subcontinent during 2017, Q. J. R. Meteorolog. Soc., 146
842   (731), https://doi.org/10.1002/qj.3688, 2853 – 2866, 2019.

843 Bhattarai, N., Mallick, K., Brunsell, N. A., Sun, G., and Jain, M.: Regional evapotranspiration
844   from an image-based implementation of the Surface Temperature Initiated Closure (STIC1.2)
845   model and its validation across an aridity gradient in the conterminous US, Hydrol. Earth Syst.
846   Sci., 22, 2311–2341, https://doi.org/10.5194/hess-22-2311-2018, 2018.

847 Bhattarai, N., Mallick, K., Stuart, J., Vishwakarma, B., Niraula, R., Sen, S. and Jain, M.: An
848   automated multi-model evapotranspiration mapping framework using remotely sensed and
849   reanalysis data, Remote Sens. Environ., 229, 69 – 92,
850   https://doi.org/10.1016/j.rse.2019.04.026, 2019.

851 Boegh, E., Soegaard, H., Christensen, J. H., Hasager, C. B., Jensen, N.O. and Nielsen, N. W.:
852   Combining weather prediction and remote sensing data for the calculation of
853   evapotranspiration rates: application to Denmark, Int. J. Remote Sens., 25, 2553 – 2574,
854   https://doi.org/10.1080/01431160310001647984, 2004.

855   Cammalleri, C. and Vogt, J.: On the Role of Land Surface Temperature as Proxy of Soil Moisture
856   Status for Drought Monitoring in Europe, Remote Sens., 7(12), 16849 – 16864,
857   https://doi.org/10.3390/rs71215857, 2015.

858   Cano, D., Monget, J., Albuisson, M., Guillard, H., Regas, N. and Wald, L.: A method for the
859   determination of the global solar radiation from meteorological satellite data. Solar Energy,
860   37(1), 840, 31 – 39, https://doi.org/10.1016/0038-092X(86)90104-0, 1986.

861   Castelli, F., Entekhabi, D. and Caporali, E.: Estimation of surface heat flux and an index of soil
862   moisture using adjoint-state surface energy balance, Water Resour. Res., 35(10), 3115 – 3125,
863   https://doi.org/10.1029/1999WR900140, 1999.

864   Dare-Idowu, O., Brut, A., Cuxart, J., Tallec, T., Rivalland, V., Zawilski, B., Ceschia, E. and
865   Jarlan, L.: Surface energy balance and flux partitioning of annual crops in south-western
866   France. Agric. For. Meteorol., 308 – 309, 108529,
867   https://doi.org/10.1016/j.agrformet.2021.108529, 2021.

868   Didan, K.: MOD13Q1 MODIS/Terra Vegetation Indices 16-Day L3 Global 250m SIN Grid
869   V006., distributed by NASA EOSDIS Land Processes DAAC,
870   doi:10.5067/MODIS/MOD13Q1.006, 2021-06-06, 2015.

871   Donohue, R. J., Hume, I. H., Roderick, M. L., McVicar, T. R., Beringer, J., Hutley, L. B., Arndt,
872   S. K.: Evaluation of the remote-sensing-based DIFFUSE model for estimating photosynthesis
873   of vegetation, Remote Sens. Environ, 155, 349–365, doi:10.1016/j.rse.2014.09.007, 2014.

874   Duan, A., Wang, M., Lei, Y. and Cui, Y.: Trends in summer rainfall over China associated with
875   the Tibetan Plateau sensible heat source during 1980–2008, J. Clim., 26, 261–275,
876   https://doi.org/10.1175/JCLI-D-11-00669.1, 2013.

877   Duan, S., Li, Z., Cheng, J. and Leng, P.: Cross-satellite comparison of operational land surface
878   temperature products derived from MODIS and ASTER data over bare soil surfaces. ISPRS
879   J. Photogramm. Remote Sens., 126, 1-10, https://doi.org/10.1016/j.isprsjprs.2017.02.003,
880   2017.

881   Eswar, R., Sekhar, M., Bhattacharya, B. and Bandyopadhyay, S.: Spatial Disaggregation of Latent
882   Heat Flux Using Contextual Models over India, Remote Sens., 9(9), 949,
883   https://doi.org/10.3390/rs9090949, 2017.

884   Friedl, M., McIver, D., Hodges, J., Zhang, X., Muchoney, D., Strahler, A., Woodcock, C., Gopal,
885   S., Schneider, A., Cooper, A., Baccini, A., Gao, F. and Schaaf, C.: Global land cover mapping

from MODIS: algorithms and early results, Remote Sens. Environ., 83(1-2), 287 – 302, https://doi.org/10.1016/S0034-4257(02)00078-0, 2002.

Gao, Z., Horton, R. andLiu, H. P.:Impact of wave phase difference between soil surface heat flux and soil surface temperature on soil surface energy balance closure, J. Geophys. Res., 115, D16112, doi:10.1029/2009JD013278, 2010.

Hillel, D.: Introduction to Soil Physics, San Diego, US, ISBN 9780123485205, 1982.

Hulley, G., Malakar, N., and Freepartner, R.: Moderate Resolution Imaging Spectroradiometer (MODIS) Land Surface Temperature and Emissivity Product (MxD21) Algorithm Theoretical Basis Document Collection-6. Pasadena, California: Jet Propulsion Laboratory, California Institute of Technology, 2016

Isaac, P., Cleverly, J., McHugh, I., van Gorsel, E., Ewenz, C., and Beringer, J.: OzFlux data: network integration from collection to curation, Biogeosciences, 14, 2903–2928, doi:10.5194/bg-14-2903-2017, 2017.

Jarvis, P.G. and McNaughton, K.G.: Stomatal Control of Transpiration – Scaling up from Leaf to Region, Adv. Ecol. Res., 15, 1-49, https://doi.org/10.1016/S0065-2504(08)60119-1, 1986.

Johansen, O.: Thermal conductivity of soils, PhD Thesis, University of Trondheim. Hanover, NH: Cold Regions Research and Engineering Laboratory, US Army Corps of Engineers, CRREL Draft English translation, https://apps.dtic.mil/sti/pdfs/ADA044002.pdf, 1975.

Johnston, M., Andreu, A., Verfaillie, J., Baldocchi, D., and Moorcroft, P.: What lies beneath: Vertical temperature heterogeneity in a Mediterranean woodland savanna, Remote Sens. Environ., https://doi.org/10.1016/j.rse.2022.112950, 2022.

Kiptala, J., Mohamed, Y., Mul, M. and Van der Zaag, P.: Mapping evapotranspiration trends using MODIS and SEBAL model in a data scarce and heterogeneous landscape in Eastern Africa, Water Resour. Res., 49(12), 8495 – 8510, https://doi.org/10.1002/2013WR014240, 2013.

Kustas, W. and Anderson, M.: Advances in thermal infrared remote sensing for land surface modeling, Agric. For. Meteorol., 149 (12), 2071 – 2081, https://doi.org/10.1016/j.agrformet.2009.05.016, 2009.

Lagouarde J.-P., Bhattacharya BK, Crébassol P., Gamet P., Babu SS, Boulet G., Briottet X., Buddhiraju KM, Cherchali S., Dadou I., Dedieu G., Gouhier M., Hagolle O Irvine M., Jacob F., Kumar A., Kumar KK, Laignel B., Mallick K., Murthy CS, Olioso A., Ottle C., Pandya

917   MR, Raju PV, Roujean J.-L., Sekhar M., Shukla MV, Singh SK, Sobrino J., Ramakrishnan
918   R.: The Indian-French Trishna Mission: Earth Observation in the Thermal Infrared with High
919   Spatio-Temporal Resolution, IGARSS 2018 - 2018 IEEE International Geoscience and
920   Remote Sensing Symposium, Institute of Electrical and Electronics Engineers (IEEE). USA,
921   4078-4081, doi:10.1109/IGARSS.2018.8518720, 2018.

922 Lagouarde, J., Bhattacharya, B., Crébassol, P., Gamet, P., Adlakha, D., Murthy, C., Singh, S.,
923   Mishra, M., Nigam, R., Raju, P., Babu, S., Shukla, M., Pandya, M., Boulet, G., Briottet, X.,
924   Dadou, I., Dedieu, G., Gouhier, M., Hagolle, O., Irvine, M., Jacob, F., Kumar, K., Laignel,
925   B., Maisongrande, P., Mallick, K., Olioso, A., Ottlé, C., Roujean, J., Sobrino, J.,
926   Ramakrishnan, R., Sekhar, M. and Sarkar, S.: Indo-French high-resolution thermal infrared
927   space mission for earth natural resources assessment and monitoring – concept and definition
928   of TRISHNA, ISPRS - International Archives of the Photogrammetry, Remote Sensing and
929   Spatial Information Sciences, XLII-3/W6, 403-407, 2019.

930 Lu, L., Zhang, T., Wang, T. and Zhou, X.: Evaluation of Collection-6 MODIS Land Surface
931   Temperature Product Using Multi-Year Ground Measurements in an Arid Area of Northwest
932   China, Remote Sens., 10(11), 1852, https://doi.org/10.3390/rs10111852, 2018.

933 Mallick, K.,& Bhattacharya, B.K., Chaurasia, S., Dutta, S., Nigam, R., Mukherjee J., Banerjee,
934   S., Kar, G., Rao, V.,Gadgil, A.., Parihar, J.: Evapotranspiration using MODIS data and limited
935   ground observations over selected agroecosystems in India, Int. J. Remote Sens., 28 (10),
936   2091 – 2110, https://doi.org/10.1080/01431160600935620, 2007.

937 Mallick, K., Bhattacharya, B. K., Rao, V. U. M., Reddy, D.R., Banerjee, S., Venkatesh, H. ,
938   Pandey, V., Kar, G., Mukherjee, J., Vyas, S., Gadgil, A.S., Patel, N.K.: Latent heat flux
939   estimation in clear sky days over Indian agroecosystems using noontime satellite remote
940   sensing data, Agric. For. Meteorol., 149 (10), 1646 – 1665,
941   https://doi.org/10.1016/j.agrformet.2009.05.006, 2009.

942 Mallick, K., Boegh, E., Trebs, I., Alfieri, J., Kustas, W., Prueger, J., Niyogi, D., Das, N., Drewry,
943   D., Hoffmann, L. and Jarvis, A.: Reintroducing radiometric surface temperature into the
944   Penman-Monteith formulation, Water Resour. Res., 51(8), 6214 – 6243,
945   https://doi.org/10.1002/2014WR016106, 2015a.

946 Mallick, K., Jarvis, A., Boegh, E., Fisher, J., Drewry, D., Tu, K., Hook, S., Hulley, G., Ardö, J.,
947   Beringer, J., Arain, A. and Niyogi, D.: A Surface Temperature Initiated Closure (STIC) for

surface energy balance fluxes, Remote Sens. Environ., 141, 243 – 261, https://doi.org/10.1016/j.rse.2013.10.022, 2014.

Mallick, K., Jarvis, A., Wohlfahrt, G., Kiely, G., Hirano, T., Miyata, A., Yamamoto, S., and Hoffmann, L.: Components of near-surface energy balance derived from satellite soundings – Part 1: Noontime net available energy, Biogeosci., 12, 433–451, https://doi.org/10.5194/bg-12-433-2015, 2015b.

Mallick, K., Toivonen, E., Trebs, I., Boegh, E., Cleverly, J., Eamus, D., Koivusalo, H., Drewry, D., Arndt, S., Griebel, A., Beringer, J. and Garcia, M.: Bridging thermal infrared sensing and physically-based evapotranspiration modeling: from theoretical implementation to validation across an aridity gradient in Australian ecosystems, Water Resour. Res., 54 (5), 3409 – 3435, https://doi.org/10.1029/2017WR021357, 2018a.

Mallick, K., Trebs, I., Boegh, E., Giustarini, L., Schlerf, M., Drewry, D., Hoffmann, L., von Randow, C., Kruijt, B., Araùjo, A., Saleska, S., Ehleringer, J., Domingues, T., Ometto, J., Nobre, A., de Moraes, O., Hayek, M., Munger, J. and Wofsy, S.: Canopy-scale biophysical controls of transpiration and evaporation in the Amazon Basin, Hydrol. Earth Syst. Sci., 20, 4237 – 4264, doi:10.5194/hess-20-4237-2016, 2016.

Mallick, K., Wandera, L., Bhattarai, N., Hostache, R., Kleniewska, M. and Chormanski, J.: A Critical Evaluation on the Role of Aerodynamic and Canopy–Surface Conductance Parameterization in SEB and SVAT Models for Simulating Evapotranspiration: A Case Study in the Upper Biebrza National Park Wetland in Poland, Water, 10 (12), 1753, https://doi.org/10.3390/w10121753, 2018b.

Mallick, K., Baldocchi, D., Jarvis, A., Hu, T., Trebs, I., Sulis, M., et al.: Insights into the aerodynamic versus radiometric surface temperature debate in thermal-based evaporation modeling. Geophys. Res. Let., 49, e2021GL097568. https://doi.org/10.1029/2021GL097568, 2022.

Maltese, A., Bates, P., Capodici, F., Cannarozzo, M., Ciraolo, G. and La Loggia, G.: Critical analysis of thermal inertia approaches for surface soil water content retrieval, Hydrol. Sci. J., 58(5), 1144 – 1161, https://doi.org/10.1080/02626667.2013.802322, 2013.

Martel, M., Glenn, A., Wilson, H. and Kröbel, R.: Simulation of actual evapotranspiration from agricultural landscapes in the Canadian Prairies, J. Hydrol. Reg. Stud., 15, 105 – 118, https://doi.org/10.1016/j.ejrh.2017.11.010, 2018.

979   Matheny, A., Bohrer, G., Stoy, P., Baker, I., Black, A., Desai, A., Dietze, M., Gough, C., Ivanov,
980   V., Jassal, R., Novick, K., Schäfer, K. and Verbeeck, H.: Characterizing the diurnal patterns
981   of errors in the prediction of evapotranspiration by several land-surface models: An NACP
982   analysis, J. Geophys. Res. Biogeosci., 119 (7), 1458 – 1473,
983   https://doi.org/10.1002/2014JG002623, 2014.

984   Minasny, B.& Hartemink, A. E.: Predicting soil properties in the tropics. Earth-Science Rev.,1 –
985   2, 52 – 62, https://doi.org/10.1016/j.earscirev.2011.01.005, 2011.

986   Mihailovic, D. T., Kallos, G., Aresenic, I.D., Lalic, B., Rajkovic, B. and Papadopoulos, A.:
987   Sensitivity of soil surface temperature in a Force-Restore Equation to heat fluxes and deep
988   soil temperature. Intl. J. Climatol., 19, 1617 – 1632, 1999.

989   Monteith, J &Unsworth, M.: Principles of Environmental Physics: Plants, Animals, and the
990   Atmosphere, Fourth Edition, 1-401, 2013.

991   Moran, M. S., Jackson, R. D., Raymond, L. H., Gay, L. W. and Slater, P. N.: Mapping surface
992   energy balance components by combining landsat thematic mapper and ground-based
993   meteorological data, Remote Sens. Environ., 30, 77 – 87, https://doi.org/10.1016/0034-
994   4257(89)90049-7, 1989.

995   Morisson, R., Angadi, S. S., Cooper, H. M., Evans, J. G., Rees, G., Sekhar, M., Taylor, C.,
996   Tripathi, S. N. and Turner, A. G. : Energy and carbon dioxide fluxes, meteorology and soil
997   physics observed at INCOMPASS land surface stations in India, 2016 to 2017, NERC
998   Environmental Information Data Centre, doi:10.5285/78c64025-1f8d-431cbdeb-
999   e69a5877d2ed, 2019b.

1000 Morisson, R., Angadi, S. S., Cooper, H. M., Evans, J., Rees, G., Sekhar, M., Taylor, C., Tripathi,
1001   S. N. and Turner, A. G. : High temporal resolution meteorology and soil physics observations
1002   from INCOMPASS land surface stations in India, 2016 to 2018, NERC Environmental
1003   Information Data Centre, doi:10.5285/c5e72461-c61f-4800- 8bbf-95c85f74c416, 2019a.

1004 Murray, T. and Verhoef, A.: Moving towards a more mechanistic approach in the determination
1005   of soil heat flux from remote measurements, Agric. For. Meteorol., 147(1-2), 80 – 87,
1006   https://doi.org/10.1016/j.agrformet.2007.06.009, 2007.

1007 Norman, J., Anderson, M., Kustas, W., French, A., Mecikalski, J., Torn, R., Diak, G., Schmugge,
1008   T. and Tanner, B.: Remote sensing of surface energy fluxes at 10^1-m pixel resolutions, Water
1009   Resour. Res. 39(8), https://doi.org/10.1029/2002WR001775, 2003.

1010   Purdy, A., Fisher, J., Goulden, M. and Famiglietti, J.: Ground heat flux: An analytical review of
1011   6 models evaluated at 88 sites and globally, J. Geophys. Res.: Biogeosci., 121(12), 3045 –
1012   3059,https://doi.org/10.1002/2016JG003591, 2016.

1013   Raja, P., Singh, M., Singh, N., and Sinha, N.K.: Photosynthesis and Biomass studies in
1014   Lasiurussindicus of Chandan Grassland in Thar Desert, XXIII International Grassland
1015   Conference, New Delhi, Volume: IGC 2015, 2015.

1016   Santanello, J. and Friedl, M.: Diurnal Covariation in Soil Heat Flux and Net Radiation, J. Appl.
1017   Meteorol.,   42(6),   851   –   862,   https://doi.org/10.1175/1520-
1018   0450(2003)042<0851:DCISHF>2.0.CO;2, 2003.

1019   Schmid, H.P.: Footprint modelling for vegetation atmosphere exchange studies: a review and
1020   perspective. Agric. For. Meteorol., 113, 159 – 183, 2002.

1021   Sauer T.J. and Horton, R.: Soil Heat flux, Micrometeorology in Agricultural Systems, Agronomy
1022   Monograph no. 47, American Society of Agronomy, Crop Science Society of America, Soil
1023   Science Society of America, 677 S. Segoe Rd., Madison, WI 53711, USA, 2005.

1024   Schaaf, C., Gao, F., Strahler, A., Lucht, W., Li, X., & Tsang, T. , trugnell, N. C., Zhang, X., Jin,
1025   Y., Muller, J., Lewis, P., Barnsley, M., Hobson, P., Disney, M., Roberts, G., Dunderdale, M.,
1026   Doll, C., d'Entremont, R. P., Hu, B., Liang, S., Privette, J. L. and Roy, D. : First operational
1027   BRDF, albedo nadir reflectance products from MODIS, Remote Sens. Environ., 83(1-2), 135
1028   – 148, doi:10.1016/s0034-4257(02)00091-3, 2002.

1029   Schymanski, S. J., Breitenstein, D., and Or, D.: Technical note: An experimental set-up to measure
1030   latent and sensible heat fluxes from (artificial) plant leaves, Hydrol. Earth Syst. Sci., 21, 3377–
1031   3400, https://doi.org/10.5194/hess-21-3377-2017, 2017.

1032   Singh, A.: Integrated Water Management: Water and Plant Growth,1–16, 2007.

1033   Sharfinezhadazizi, Z., Nobouzi, H., Prakash, S., Beale, C., and Khanbilvardi, R.: A global analysis
1034   of land surface temperature diurnal cycle using MODIS observations, J. Appl. Meteorol.
1035   Climatol., 58, 1279 – 1291, doi:10.1175/JAMC-D-18-0256.1, 2019.

1036   Stoy, P., Mauder, M., Foken, T., Marcolla, B., Boegh, E., Ibrom, A., Arain, M., Arneth, A.,
1037   Aurela, M., Bernhofer, C., Cescatti, A., Dellwik, E., Duce, P., Gianelle, D., van Gorsel, E.,
1038   Kiely, G., Knohl, A., Margolis, H., McCaughey, H., Merbold, L., Montagnani, L., Papale, D.,
1039   Reichstein, M., Saunders, M., Serrano-Ortiz, P., Sottocornola, M., Spano, D., Vaccari, F. and
1040   Varlagin, A.:A data-driven analysis of energy balance closure across FLUXNET research

sites: The role of landscape scale heterogeneity, Agric. For. Meteorol., 171 – 172, 137 – 152, https://doi.org/10.1016/j.agrformet.2012.11.004, 2013.

Su, Z.: The Surface Energy Balance System (SEBS) for estimation of turbulent heat fluxes, Hydrol. Earth Syst. Sci., 6, 85–100, doi:10.5194/hess-6-85-2002, 2002.

Tian, L., Zhang, Y., & Zhu, J.: Decreased surface albedo driven by denser vegetation on the Tibetan Plateau, Environ. Res. Lett., 9 (10), 104001, doi:10.1088/1748-9326/9/10/104001, 2014.

Trebs, I., Mallick, K., Bhattarai, N., Sulis, M., Cleverly, J., Woodgate, W., Silberstein, R., Najera, H.-N., Beringer, J., Meyer, W. S., Su, Z., and Boullet, G.: The role of aerodynamic resistance in thermal remote sensing-based evapotranspiration models, Remote Sens. Environ., 264, 112602, doi:10.1016/j.rse.2021.112602, 2021

Tsuang, B.: Ground Heat Flux Determination according to Land Skin Temperature Observations from i*n-situ* Stations and Satellites, J. Hydrometeorol., 6 (4), 371 – 390, https://doi.org/10.1175/JHM425.1, 2005.

Turner, A., Bhat, G., Martin, G., Parker, D., Taylor, C., Mitra, A., Tripathi, S., Milton, S., Rajagopal, E., Evans, J., Morrison, R., Pattnaik, S., Sekhar, M., Bhattacharya, B., Madan, R., Govindankutty, M., Fletcher, J., Willetts, P., Menon, A. and Marsham, J.: Interaction of convective organization with monsoon precipitation, atmosphere, surface and sea: The 2016 INCOMPASS field campaign in India, Q. J. R. Meteorolog. Soc., 1–25, https://doi.org/10.1002/qj.3633, 2019.

Van Dijk, A.I.J.M., Gash, J.H., Gorsel, E.V., Blanken, P.D., Cescatti, A., Emmel, C., Gielen, B., Harman, I.N., Kiely,G., Merbold, L., Montagnani, L., Moors, E., Sottocornola, M., Varlagin, A., Williams, C.A., Wohlfahrt, G.: Rainfall interception and the coupled surface water and energy balance, Agric For Meteorol., 214 – 215, 402 – 415, https://doi.org/10.1016/j.agrformet.2015.09.006, 2015.

Van Genuchten, M.: A Closed-form Equation for Predicting the Hydraulic Conductivity of Unsaturated Soils, Soil Sci. Soc. Am. J., 44 (5), 892, https://doi.org/10.2136/sssaj1980.03615995004400050002x, 1980.

Venturini, V., Islam, S. and Rodriguez, L.: Estimation of evaporative fraction and evapotranspiration from MODIS products using a complementary based model, Remote Sens. Environ., 112(1), 132 – 141, doi:10.1016/j.rse.2007.04.014,2008.

1072   Verhoef, A., Ottlé, C., Cappelaere, B., Murray, T., Saux-Picart, S., Zribi, M., Maignan, F.,
1073   Boulain, N., Demarty, J. and Ramier, D.: Spatio-temporal surface soil heat flux estimates from
1074   satellite data; results for the AMMA experiment at the Fakara (Niger) supersite, Agric. For.
1075   Meteorol., 154-155, 55 – 66, doi:10.1016/j.agrformet.2011.08.003,2012.

1076   Verhoef, A.: Remote estimation of thermal inertia and soil heat flux for bare soil, Agric. For.
1077   Meteorol., 123(3-4), 221 – 236, doi:10.1016/j.agrformet.2003.11.005,2004.

1078   Vesala, T., Kljun, N., Rannik, U., Rinne, A. Sogachev, Markkanen, T., Sabelfeld, K., Foken, T.
1079   and Leclerc, M.Y.: Flux and concentration footprint modelling: State of the art. Environ.
1080   Polln., 152, 653 – 666, 2008.

1081   Wan, Z.: New refinements and validation of the collection-6 MODIS land-surface
1082   temperature/emissivity product, Remote Sens. Environ., 140, 36 – 45,
1083   doi:10.1016/j.rse.2013.08.027, 2014.

1084   Wang, S., Yang, Y., Luo, Y., and Rivera, A.: Spatial and seasonal variations in evapotranspiration
1085   over Canada's landmass, Hydrol. Earth Syst. Sci., 17, 3561–3575, doi:10.5194/hess-17-3561-
1086   2013, 2013.

1087   Wilson, K., Goldstein, A., Falge, E., Aubinet, M., Baldocchi, D., Berbigier, P., Bernhofer, C.,
1088   Ceulemans, R., Dolman, H., Field, C., Grelle, A., Ibrom, A., Law, B., Kowalski, A., Meyers,
1089   T., Moncrieff, J., Monson, R., Oechel, W., Tenhunen, J., Valentini, R. and Verma, S.: Energy
1090   balance closure at FLUXNET sites, Agric. For. Meteorol., 113(1-4), 223 – 243,
1091   doi:10.1016/S0168-1923(02)00109-0,2002.

1092   Winter, J. and Eltahir, E.: The Sensitivity of Latent Heat Flux to Changes in the Radiative Forcing:
1093   A Framework for Comparing Models and Observations, J. Clim., 23(9),2345-2356,
1094   doi:10.1175/2009JCLI3158.1,2010.

1095   Zerefos, C. S. & Bais, A. F.: Solar Ultraviolet Radiation: Modelling, Measurements and
1096   Effects, Springer Berlin Heidelberg, 2013.

1097

1098

1099

1100

1101

1102 **Appendix A**

1103 **Table A1: A list of symbols, their descriptions and units used in the present study**

Attributes	Symbol	Description
Temperature	T_A	Air temperature (^oC)
	T_{Max}	Maximum air temperature (^oC)
	T_{Min}	Minimum air temperature (^oC)
	T_D	Air dew-point temperature (^oC)
	T_{STA}	point-scale soil temperature amplitude
	ΔTs	noon-night LST difference (^oC)
	T_{ST}	Soil temperature (^oC)
	T_S	Land surface temperature (LST) (^oC)
Humidity, vapor pressures	R_H	Relative humidity (%)
	e_A	Atmospheric vapor pressure at the level of T_A measurement (hPa)
	e_A^*	Saturation vapor pressure at the level of T_A measurement (hPa)
	e_S^*	Saturation vapor pressure at surface (hPa)
	D_A	Atmospheric vapor pressure deficit at the level of T_A measurement (hPa)
Radiation	R_G	Downwelling shortwave radiation (or global radiation) (W m^{-2})
	R_R	Upwelling or reflected shortwave radiation (W m^{-2})
	$R_L\downarrow$	Downwelling longwave radiation (W m^{-2})
	$R_L\uparrow$	Upwelling longwave radiation (W m^{-2})
	τ_{sw}	Atmospheric transmissivity for shortwave radiation (unitless)
	α_R	Broadband shortwave surface albedo (unitless)
SEB components	LE_i	Latent heat flux (W m^{-2}); subscript 'i' signifies 'instantaneous'
	H_i	Sensible heat flux (W m^{-2}); subscript 'i' signifies 'instantaneous'
	G_i	Ground heat flux (W m^{-2}); subscript 'i' signifies 'instantaneous'
	R_{Ni}	Net radiation (W m^{-2}); subscript 'i' signifies 'instantaneous'
	ϕ	Net available energy (W m^{-2}); i.e., $R_N - G$
	A	Ecosystem-scale surface soil temperature amplitude (^oC)

MV2007 model	T_{Sd}	Daytime T_S (^{o}C)
	T_{Sn}	Nighttime T_S (^{o}C)
	ω	Angular frequency (rad s^{-1})
	ϕ'_n	Phase shift of the nth soil surface temperature harmonic (rad)
	Δ	Shape parameter (unitless)
	S_r	Relative soil moisture saturation (m^3 m^{-3})
	f_s	Sand fraction (unitless)
	θ_{fc}	Soil water content at field capacity (m^3 m^{-3})
	θ_{wp}	Soil water content at permanent wilting point (m^3 m^{-3})
	θ_*	Soil porosity (cm^3 cm^{-3})
	J_S	Summation of harmonic terms of soil surface temperature (K)
	Υ'	Soil textural parameter (unitless)
	Γ	Soil thermal inertia (J K^{-1} m^{-2} s$^{-0.5}$)
	τ_0	Thermal inertia of air-dry soil (J K^{-1} m^{-2} s$^{-0.5}$)
	τ_*	Thermal inertia of saturated soil (J K^{-1} m^{-2} s$^{-0.5}$)
	t'	Time of satellite overpass (seconds)
	Δt	Time offset between the canopy composite temperature and the below-canopy soil surface temperature (seconds)
	κ	Total number of harmonics used (unitless)
	f_c	Vegetation fraction (unitless)
	θ	Volumetric soil moisture (cm cm^{-3})
Clear-sky R_{Ni} model	R_{ns}	Net shortwave radiation (W m^{-2})
	R_{nl}	Net long wave radiation (W m^{-2})
	G_{sc}	Solar constant (1367 W m^{-2})
	β_e	Sun elevation angle (^{0}).
	ε_s	Infrared surface emissivity (unitless)
	ε_a	Atmospheric emissivity (unitless)
	E	Eccentricity correction factor due to variation in Sun-Earth distance (unitless)
	M	Aggregated moisture availability (0-1)

STIC-TI model	g_A	Aerodynamic conductance (m s^{-1})
	g_S	Canopy-surface conductance (m s^{-1})
	T_0	Aerodynamic temperature (or source/sink height temperature) (^{o}C)
	T_{0D}	Dewpoint temperature at the source/sink height (^{o}C)
	Λ	Evaporative fraction (unit less)
	e_0	Vapor pressure at the source/sink height (hPa)
	e_0^*	Saturation vapor pressure at the source/sink height (hPa)
	D_0	Vapor pressure deficit at source/sink height (hPa)
	s_1	Psychrometric slope of vapor pressure and temperature between (T_{0D} -T_D) versus (e_0 -e_A) (h Pa K^{-1})
	s_2	Psychrometric slope of vapor pressure and temperature between (T_S-T_D) versus (e_s^*-e_A) (h Pa K^{-1})
	s_3	Psychrometric slope of vapor pressure and temperature between (T_{0D} -T_D) versus (e_s^*-e_A).
	κ	Ratio between (e_0^* - e_A) and (e_s^* - e_A) (unitless)
	s	Slope of saturation vapor pressure vs. temperature curve (h Pa K^{-1})
	α	Priestley-Taylor coefficient (unitless)
Ancillary meteorological variables	U	Wind speed at 8 m height (m s^{-1})
	u^*	Friction velocity (m s^{-1})
Constants	P	Precipitation (mm d^{-1})
	γ	Psychrometric constant (h Pa k^{-1})
	c_p	Specific heat capacity of air at constant pressure (MJ kg^{-1} K^{-1})
	ρ	Density of air (Kg m^{-3})
	σ	Stefan–Boltzmann constant (5.67 x 10^{-8} Wm^{-2}K^{-4})
Sensor view geometry	VZA	MODIS Aqua sensor view angle (°)
	δVZA	Difference in MODIS Aqua day-night sensor view angle (°)

1104

1105

1106 **Table A2:** Summary of instruments used, height or depth and period of measurements, measured

1107 variables at nine EC flux tower sites

Type of primary instruments used for in situ data recording at flux tower sites	Measurement height/ depth (m)	Measured variables
Net radiometer	• 3m (IND-Naw, IND-Jai, IND-Sam) • 15m (AU-Ade) • 12.2m (AU-ASM) • 23m (AU-How)2m (US-Ton, US-Var)	Four radiation flux components: shortwave incoming (R_G) and outgoing (R_R); longwave incoming ($R_L\downarrow$) and outgoing ($R_L\uparrow$)
EC assembly with IRGA (Infrared Gas Analyzer), three-dimensional sonic anemometer, TC probe	• 8m (IND-Naw; IND-Jai; IND-Sam) • 4.5m (IND-Dha) • 15m (AU-Ade) • 11.6m(AU-ASM) • 23m (AU-How) • 2m (US-Ton, US-Var)	High response wind vectors (*u*, *v* and *w)*, sonic temperature, and CO_2- water vapor mass at 10/20 Hz frequency
Humidity and temperature probe	• 8m (IND-Naw, IND-Jai, IND-Sam) • 4.5m (IND-Dha) • 15m (AU-Ade), 11.6m (AU-ASM) • 23m (AU-How), 70m (AU-How) • 2m (US-Ton, US-Var)	T_A and R_H
Soil temperature probe	• -0.1m (IND-Dha) • -0.15m (AU-Ade) • (-0.02, -0.06m) (AU- ASM) • -0.08m (AU- How) • -0.02m, -.04m, -0.08m, and -0.16m (US-Ton, US-Var)	T_{ST}
Soil heat flux plates	• Ground, 0.1 m (IND-Dha) • Ground, -0.15 m (AU-Ade) • Ground, -0.08 m (AU-ASM) • Ground, -0.15 m (AU-How) • -0.01m (US-Ton, US-Var)	Soil heat flux (G)

1108 **Appendix B**

1109 **B1: Clear-sky instantaneous net radiation (R_{Ni}) model**

1110 Net radiation (R_N) is defined as the difference between the incoming and outgoing radiation, which

1111 includes both longwave and shortwave radiation at the Earth's surface.

1112 Terrestrial R_N has four components: downwelling and upwelling shortwave radiation (R_G and R_R),

1113 downwelling and upwelling longwave radiation ($R_L\downarrow$ and $R_L\uparrow$), respectively.

$$R_N = (R_G - R_R) + (R_{L\downarrow} - R_{L\uparrow}) \tag{B1}$$

1114 Out of these four terms mentioned in eq.(B1), R_G and $R_L\downarrow$ are dependent on various factors such

1115 as geographic location, season, cloudiness, aerosol loading, atmospheric water vapor content and

1116 less on surface properties. On the other hand, the upwelling radiations in eq. (B1) strongly depends

1117 on the surface properties such as surface reflectance and emittance, land surface temperature, and

1118 soil water content (Zerefos and Bais, 2013).

1119 Instantaneous net radiation (R_{Ni}) can be derived using eq. B2 as follows (Mallick et al., 2007):

$$R_{Ni} = R_{ns} - R_{nl} \tag{B2}$$

$$R_{ns} = (1 - \alpha_R)\, R_G \tag{B3}$$

$$R_{nl} = R_{L\downarrow} - R_{L\uparrow} \tag{B4}$$

1120 Where, R_{ns} is net shortwave radiation (W m^{-2}), R_{nl} is net longwave radiation (W m^{-2}).and α_R is the

1121 broadband surface albedo shortwave spectrum.

1122 A WMO (World Meteorological Organization) shortwave radiation model (Cano et al.,1986)

1123 calibrated over Indian conditions (Mallick et al., 2007, 2009) was used to compute R_G using the

1124 following equation:

$$R_G = \tau_{sw} G_{sc} E\, (\sin\beta_e)^{1.15} \tag{B5}$$

1125 Where, τ_{sw} is the is the global clear sky transmissivity for the shortwave radiation (0.7), G_{sc} is the

1126 solar constant (1367 Wm^{-2}), ε is the eccentricity correction factor due to variation in Sun-Earth

1127 distance and β_e is the sun elevation in degrees.

1128 $R_L\downarrow$ at any instance was calculated as follows:

$$R_{L\downarrow} = \varepsilon_a\, \sigma\, (273.14 + T_A)^4 \tag{B6}$$

1129 Where, σ is the Stefan–Boltzmann constant (5.67×10^{-8} Wm^{-2}K^{-4}); T_A is the air temperature (^{0}C);

1130 ε_a is the atmospheric emissivity.

1131 Atmospheric emissivity (ε_a) was computed using the following equation (Bastiaanssen et

1132 al.,1998):

$$\varepsilon_a = 0.85 - \ln\tau_{sw}{}^{0.09} \tag{B7}$$

1133 $R_L\uparrow$ at any particular instance was calculated as follows:

$$R_{L\uparrow} = \varepsilon_s \sigma(273.14 + T_s)^4 \tag{B8}$$

1134 Where, ε_s is the surface emissivity in thermal infrared ($8 - 14$ µm) spectrum and T_S is the land

1135 surface temperature (^{0}C).

B2: Evaluation of STIC-TI R_{Ni}

1137 Comparison of the clear-sky R_{Ni} estimates with respect to *in situ* measurements revealed RMSE in

1138 R_{Ni} to the order of $27 - 72$ W m^{-2}, MAPD $8 - 24\%$, BIAS $(-67) - 50$ W m^{-2}, and R^2 varying from

1139 $0.62 - 0.90$ across all the sites (Fig. B2, Table B2). Among the nine sites, a consistent

1140 underestimation of R_{Ni} was noted in IND-Dha, US-Ton, and US-Var (with BIAS of -23 W m^{-2}, -

1141 61 W m^{-2} and -67 W m^{-2}), whereas substantial overestimation of R_{Ni} was found in IND-Sam, IND-

1142 Naw, and AU-ASM with a BIAS of 50 W m^{-2}, 37 W m^{-2} and 43 W m^{-2}, respectively (Table B2).
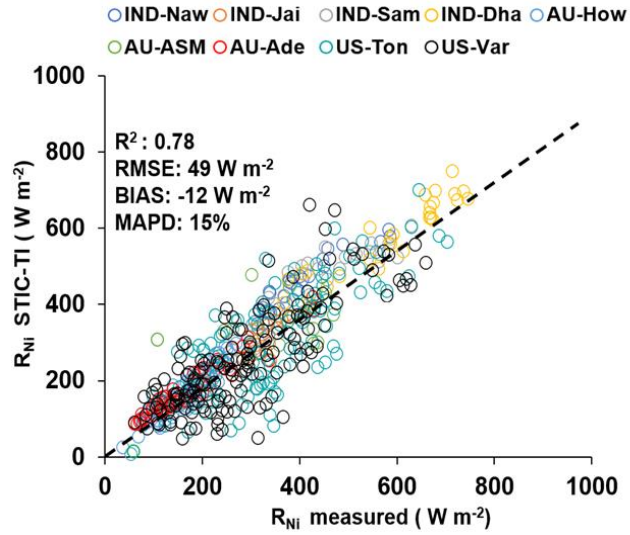
Figure B2: Validation of STIC-TI derived R_{Ni} estimates with respect to *in situ* measurements in different ecosystems. The regression equation between modeled versus in-situ R_{Ni} is, R_{Ni} (STIC-TI) = 0.78R_{Ni} (tower) +58.92.

Table B2: Performance evaluation statistics of clear-sky R_{Ni} estimates in nine different agroecosystems

Sites	Error statistics of clear-sky R_{Ni} model estimates			
	R^2	BIAS ($W\ m^{-2}$)	RMSE ($W\ m^{-2}$)	MAPD (%)
IND-Jai	0.81	-9	32	8
IND-Naw	0.81	37	56	12
IND-Dha	0.81	-23	42	9
IND-Sam	0.64	50	67	15
US-Ton	0.68	-61	69	21
US-Var	0.62	-67	72	24
Au-How	0.87	7	27	15
AU-ASM	0.88	43	50	14
AU-Ade	0.90	11	27	16

Appendix C

C1: Estimating SEB fluxes using STIC1.2 analytical model and thermal remote sensing data

1147 STIC1.2 (Mallick et al., 2014, 2015a,b, 2016, 2018a) is a one-dimensional physically based SEB

1148 model and is based on the integration of satellite LST observations into the Penman–Monteith

1149 Energy Balance (PMEB) equation (Monteith, 1965). In STIC1.2, the vegetation–substrate

1150 complex is considered as a single unit. Therefore, the aerodynamic conductances from individual

1151 air-canopy and canopy-substrate components is regarded as an 'effective' aerodynamic

1152 conductance (g_A), and surface conductances from individual canopy (stomatal) and substrate

1153 complexes is regarded as an 'effective' canopy-surface conductance (g_S) which simultaneously

1154 regulate the exchanges of sensible and latent heat fluxes (H and LE) between surface and

1155 atmosphere. One of the fundamental assumptions in STIC1.2 is the first order dependence of these

1156 two critical conductances on M through T_S. Such an assumption enabled an integration of satellite

1157 LST in the PMEB model (Mallick et al., 2016). The common expression for LE and H according

1158 to the PMEB equation is as follows:

$$LE = \frac{s\phi + \rho c_P g_A D_A}{s + \gamma\left(1 + \frac{g_A}{g_S}\right)} \tag{C6}$$

$$H = \frac{\gamma\phi\left(1 + \frac{g_A}{g_S}\right) - \rho c_P g_A D_A}{s + \gamma\left(1 + \frac{g_A}{g_S}\right)} \tag{C7}$$

1159 In the above equations, the two biophysical conductances (g_A and g_S) are unknown and the

1160 STIC1.2 methodology is based on finding analytical solutions for the two unknown conductances

1161 to directly estimate LE (Mallick et al., 2016, 2018a). The need for such analytical estimation of

1162 these conductances is motivated by the fact that g_A and g_S can neither be measured at the canopy

1163 nor at larger spatial scales, and there is no universally agreed appropriate model of g_A and g_S that

1164 currently exists (Matheny et al., 2014; van Dijk et al., 2015). By integrating T_S with standard SEB

1165 theory and vegetation biophysical principles, STIC1.2 formulates multiple state equations in order

1166   to eliminate the need to use the empirical parameterizations of the g_A and g_S and also to bypass the

1167   scaling uncertainties of the leaf-scale conductance functions to represent the canopy-scale

1168   attributes. The state equations for the conductances are expressed as a function of those variables

1169   that are mostly available as remote sensing observations and weather forecasting models. In the

1170   state equations, a direct connection to T_S is established by estimating M as a function of T_S. The

1171   information of M is subsequently used in the state equations of conductances, aerodynamic

1172   variables (aerodynamic temperature, aerodynamic vapor pressure), and evaporative fraction,

1173   which is eventually propagated into their analytical solutions. M is a unitless quantity, which

1174   describes the relative wetness (or dryness) of a surface and also controls the transition from

1175   potential to actual evaporation; which implies M→1 under saturated surface conditions and M→0

1176   under extremely dry conditions. Therefore, M is critical for providing a constraint against which

1177   the conductances are estimated. Since T_S is extremely sensitive to the surface moisture variations,

1178   it is extensively used for estimating M in a physical retrieval scheme (detail in Appendix A3 of

1179   Bhattarai et al., 2018; Mallick et al., 2016, 2018a). It is hypothesized that linking M with the

1180   conductances will simultaneously integrate the information of T_S into the PMEB model. To

1181   illustrate, we express the state equations by symbols, $sv_1 = f\ \{c_1, c_2, c_3, v_1, v_2, v_3, v_4, sv_3, sv_5\}$; sv_2

1182 $= f\ \{v_4, sv_1, sv_5, sv_6\}$; $sv_3 = f\ \{c_3, v_3, v_4, sv_4, sv_5\}$; $sv_4 = f\ \{c_3, v_3, sv_1, sv_2, sv_7, sv_8\}$. Here, f, sv, v,

1183   and c denote the function, state variables, input variables (5 input variables; radiative and

1184   meteorological), and constants (3 constants), respectively. Here sv_1 to sv_4 are g_A, g_S, aerodynamic

1185   temperature (T_0), evaporative fraction (Λ), and sv_8 is M. Given the estimates of M, net radiative

1186   energy ($R_{N\,i} - G_i$), T_A, R_H, the four state equations are solved simultaneously to derive analytical

1187   solutions for the four state variables and to produce a surface energy balance "closure" that is

1188   independent of empirical parameterizations for g_A, g_S, T_0, and Λ. However, the analytical solutions

1189   to the four state equations contain three accompanying unknown state variables (effective vapor

1190   pressures at source/sink height, and Priestley-Taylor variable), and as a result there are four

1191   equations with seven unknowns. Consequently, an iterative solution was found to determine the

1192   three additional unknown variables as detailed in this section above and also described in Mallick

1193   et al. (2016, 2018a) and Bhattarai et al. (2018). The state equations of STIC are given below.

$$g_A = \frac{\phi}{\rho c_P \left[(T_0 - T_A) + \left(\frac{e_0 - e_A}{\gamma} \right) \right]} \qquad (C1)$$

$$g_S = g_A \frac{(e_0 - e_A)}{(e_0^* - e_0)} \qquad (C2)$$

$$T_0 = T_A + \left(\frac{e_0 - e_A}{\gamma} \right) \left(\frac{1 - \Lambda}{\Lambda} \right) \qquad (C3)$$

$$\Lambda = \frac{2\alpha s}{2s + 2\gamma + \gamma \frac{g_A}{g_S}(1 + M)} \qquad (C4)$$

1194   Detailed derivations of these four state equations are given in Mallick et al. (2016). Given the

1195   values of M, R_N, G, T_A, and R_H or e_A, the four state equations can be solved simultaneously to

1196   derive analytical solutions for the four unobserved variables and to simultaneously produce a

1197   'closure' of the PMEB model that is independent of empirical parameterizations for both g_A and

1198 g_S. However, the analytical solutions to the four state equations contain three accompanying

1199   unknowns; e_0 (vapor pressure at the source/sink height), e_0^* (saturation vapor pressure at the

1200   source/sink height), and Priestley-Taylor coefficient (α), and as a result there are four equations

1201   with seven unknowns. Consequently, an iterative solution was needed to determine the three

1202   unknown variables (as described in Appendix A2 in Mallick et al. 2016). Once the analytical

1203   solutions of g_A and g_S are obtained, both variables are returned into eq. (13) to directly estimate

1204   LE.

1205   In STIC-TI, an initial value of α was assigned as 1.26; initial estimates of e_0^* were obtained from

1206 T_S through temperature-saturation vapour pressure relationship, and initial estimates of e_0 were

1207   obtained from M as, $e_0 = e_A + M(e_0^* - e_A)$. Initial T_{0D} and M were estimated according to

1208   Venturini et al. (2008) as described in section 3.2, and initial estimation of G was performed from

1209   initial M using the equation sets eq. (2) – eq. (11). With the initial estimates of these variables;

1210   first estimate of the conductances, T_0, Λ, H, and LE were obtained. The process was then iterated

1211   by updating e_0^*, D_0, e_0, T_{0D}, M, and α (using eq. A9, A10, A11, A17, A16 and A15 in Mallick et

1212   al., 2016), with the first estimates of g_S, g_A, T_0, and LE, and re-computing G, ϕ, g_S, g_A, T_0, Λ, H,

1213   and LE in the subsequent iterations with the previous estimates of e_0^*, e_0, T_{0D}, M, and α until the

1214 convergence of LE was achieved. Stable values of G, conductances, LE, H, T_0, e_0^*, e_0, T_{0D}, M, and

1215 α were obtained within ~25 iterations. The inputs needed for computation of LE_i (eq.C6) are air

1216 temperature (T_A), land surface temperature (T_S), relative humidity (R_H), net radiation (R_{Ni}) and

1217 soil heat flux (G_i).

1218 **Appendix D**

1219 The temporal variation of estimated A and T_{STA} is shown in Fig. D1. The annual variations of T_{STA}

1220 in different ecosystem was found to be within the ranges of 1 - 4° C.
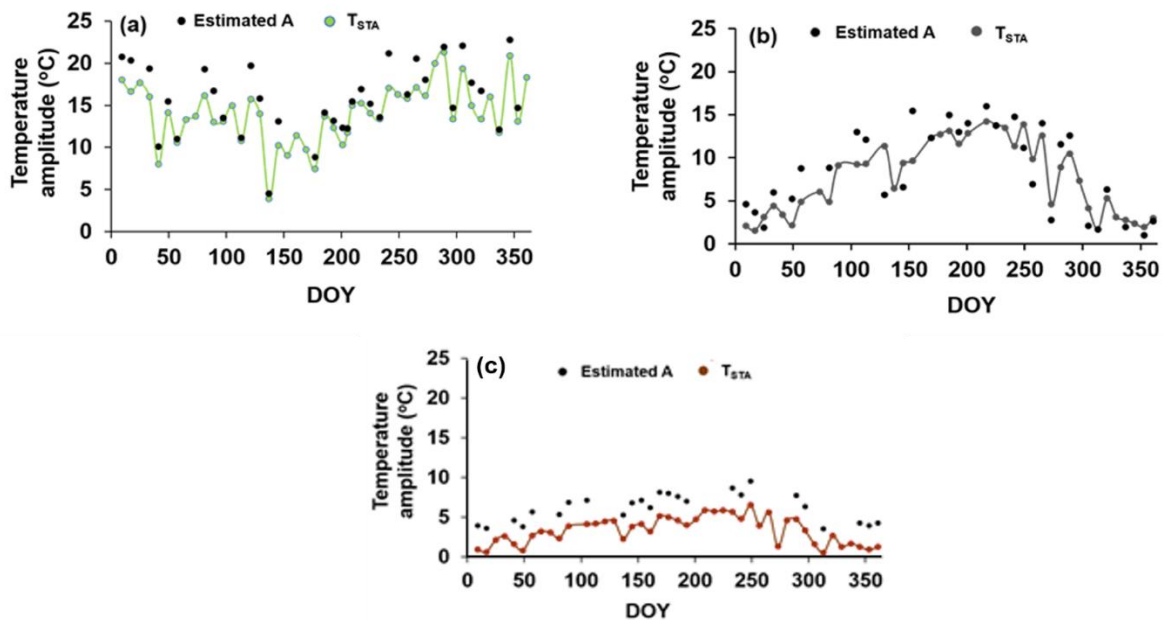
1221

1222 **<u>Figure D1</u>:** Temporal variation of A and T_{STA} in (a) AU-ASM (2013), (b) US-Ton (2014), (c) US-

1223 Var (2014)**.**


1224

1225

1226

1227

1228

1229

1230 **Appendix E**

1231 **Table E1**: Soil textural properties and their values used in the present study (Murray and Verhoef,
1232 2007; Minasny et al., 2011; Anderson et al., 2007).

Soil texture	Water retention Shape parameter (δ)	Field capacity (vol/vol) (%) θ_{fc}	Wilting point (vol/vol) (%) θ_{wp}	Sand fraction (f_s)	Saturated soil moisture (vol/vol) (%) θ_*
Sand	2.77	10	5	0.92	43
Loamy Sand	2.39	12	5	0.82	41
Sandy loam	2.27	18	8	0.58	41
Loam	2.20	28	14	0.43	43
Silty loam	2.22	31	11	0.17	45
Sandy clay loam	2.17	27	17	0.58	39
Clay loam	2.14	36	22	0.40	41
Silty clay loam	2.14	38	22	0.10	43
Sandy clay	2.11	36	25	0.52	38
Silty clay	2.12	41	27	0.06	46
Clay	2.10	42	30	0.22	38

1233　**Appendix F**

1234　Day-night view angle effect on errors of STIC-TI heat flux estimates from measurements is shown

1235　in Figure F.

(a)　　　　　　　　　　　　**(b)**

(c)
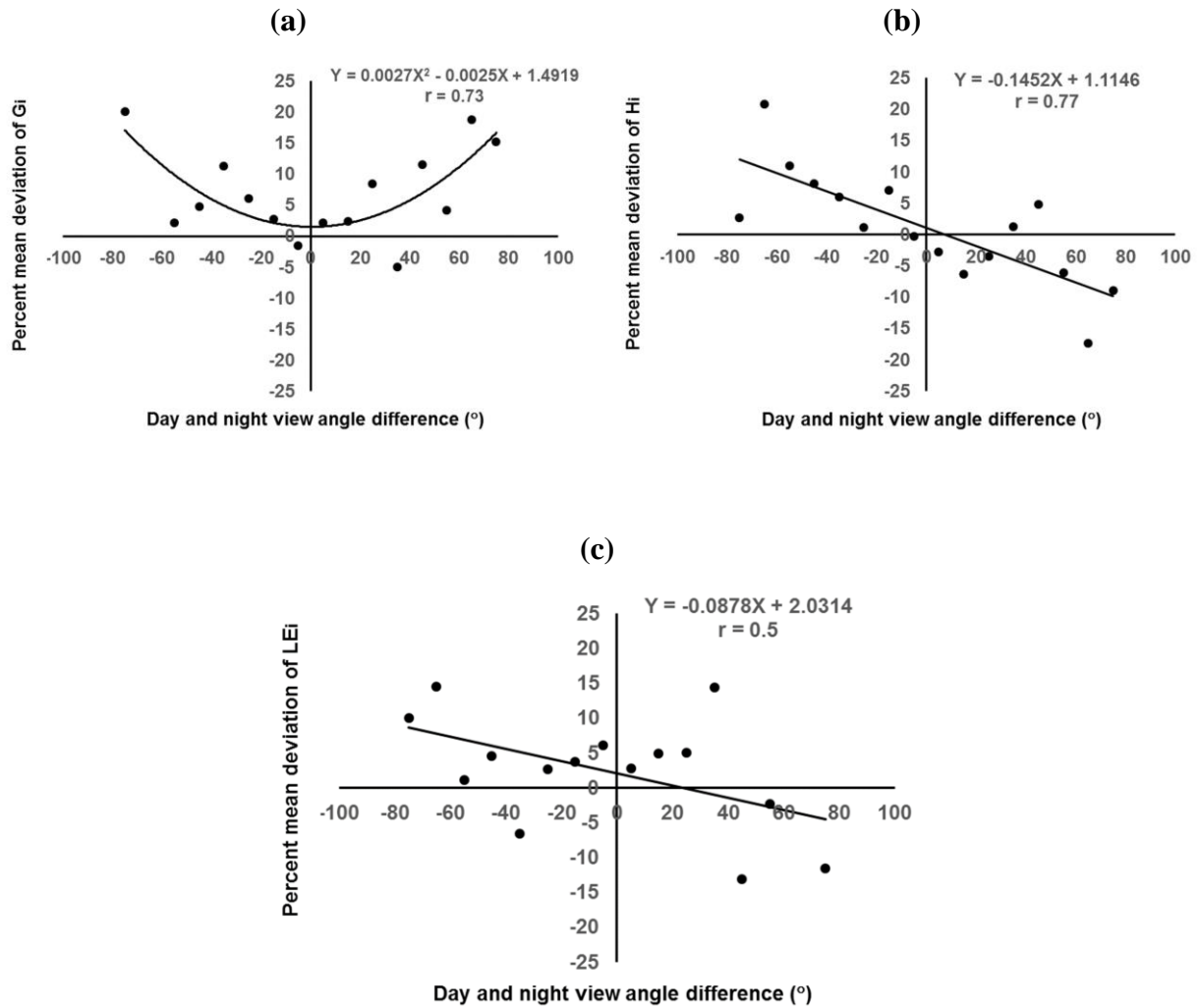
Figure F1: Dependence of STIC-TI model flux error in terms of mean percent deviation from measurements on day-night view angle difference of MODIS Aqua expressed as mean of 10° bin for (a) G_i, (b) H_i, and (c) LE_i.

1236

1237

1238